UNIVERSITY OF TARTU

Faculty of Science and Technology

Institute of Physics

HANS TERAS

ESTCUBE-2 ATTITUDE AND ORBIT CONTROL SUBSYSTEM SENSOR AND ACTUATOR CALIBRATION AND EVALUATION

Master's thesis
(30 ECTS)

Supervisors:

Riho Vendt, PhD
Hendrik Ehrpais, MSc

TARTU 2020

Abstract

ESTCube-2 attitude and orbit control subsystem sensor and actuator calibration and evaluation

This thesis presents the ESTCube-2 attitude and orbit control subsystem (AOCS) sensor and actuator testing and calibration plan, which is used to both validate the system design and evaluate its performance. This thesis presents a revision of the requirements the mission sets for the AOCS, which are used as a basis for the creation of the testing and evaluation plan of the subsystem. This thesis will then build upon the requirements and the testing plan and cover the work done so far on the testing plan, analyse the gathered data, summarize a theoretical general sensor model for the IMU, and outline the steps needed for a successful ESTCube-2 Flight Model testing campaign and a successful mission in orbit. ESTCube-2 nanosatellite is rapidly approaching the final integration campaign before launch and this thesis is a necessary step to ensure that the AOCS subsystem can enable the successful testing of the scientific payloads in-orbit.

Keywords: ESTCube-2, AOCS, ADCS, 3U, CubeSat, nanosatellite, calibration, sensors, IMU, MEMS, Sun Sensor, actuators, reaction wheel, magnetorquer

CERCS: T110 Instrumentation Technology, T320 Space Technology, P160 Statistics and Operation Research

Resümee

ESTCube-2 asendi määramise ja kontrolli alamsüsteemi sensorite ja täiturite kalibratsioon ja hindamine

Käesolev magistritöö esitab ESTCube-2 kuupsatelliidi asendi- ja orbiidikontrolli alamsüsteemi (AOCS-i) sensorite ning täiturite katsetus- ning kalibratsiooniplaani, mille abil kinnitatakse süsteemi õnnestunud disain ning antakse hinnang selle suutlikkusele. Selle magistritöö eesmärgiks on koostada ühene missioonist tulenevate nõuete komplekt AOCS-i alamsüsteemile, mis on seejärel aluseks põhjaliku katsetus- ning hindamisplaani loomisel. Antud magistritöö katab põhjalikult seni katsetusplaani käigus ning sellele eelenva tehtud töö alamsüsteemi kallal, samuti analüüsitakse kogutud andmeid, püstitatakse üldistatud ning lihtne inertsiaalanduri mudel ja visandatakse vajalikud järgnevad sammud, et kindlustada satelliidi edukas lennumudeli katsetuskampaania ning sellele järgnev missioon kosmoses. ESTCube-2 projekt on lähenemas lõpusirgele ning süsteemi lõplikule kokku integreerimisele enne raketistarti. See magistritöö on oluline samm, et tagada asendi- ja orbiidikontrolli alamsüsteemi edukus tulevaseks teadusmissiooniks Maa orbiidil.

Märksõnad: ESTCube-2, AOCS, ADCS, 3U, CubeSat, kuupsatellit, nanosatelliit, kalibratsioon, sensorid, IMU, inertsiaalandur, MEMS, Päiksesensorid, täiturid, hooratas, elektromagnettäiturid

Table of Contents

List of Figures

List of Tables

Acronyms and Abbreviations

3U – Consisting of three 10 x 10 x 10 cm x 1.3 kg units

AOCS – Attitude and Orbit Control Subsystem (on EC-2)

ADCS – Attitude Determination and Control Subsystem

CDP – Coulomb Drag Propulsion, de-orbit experiment using E-Sail in Earth's ionosphere.

CGP – Cold Gas Propulsion (butane thrusters)

COTS – Commercial Off-the-Shelf

E-Sail – Electric solar wind sail experiment on EC-2, (see also: CDP)

EC-1 – ESTCube-1 nanosatellite, launched in May 2013.

EC-2 – ESTCube-2 nanosatellite

ECSS – European Cooperation for Space Standardization

EM – Engineering Model, FlatSat for ESTCube-2

FM – Flight Model

FoV – Field of View

IMU – Inertial Measurement Unit

IOD/IOV – In-Orbit Demonstration/Verification

LEO – Low Earth Orbit (~100 to 2000 km above mean sea level)

MEMS – Microelectromechanical System

OBC – On-Board Computer

OBCS – On-Board Computer Subsystem (on EC-2)

PCB – Printed Circuit Board

RW – Reaction Wheels

SS – Sun Synchronous (a near-polar orbit precessing with a period of 1 Earth year)

UKF – Unscented Kalman Filter

Introduction

ESTCube-2 is an upcoming nanosatellite of 3U CubeSat standard with multiple payloads destined for technology demonstration on a Sun-Synchronous (SS) Low Earth Orbit (LEO). It is primarily developed by the Estonian Student Satellite Foundation in collaboration with Tartu Observatory, University of Tartu (TO) and the Finnish Meteorological Institute, who also provide the primary experimental payloads: the plasma-break experiment and two Earth observation cameras. For ESTCube-2, a calibrated and highly functional Attitude and Orbit Control Subsystem (AOCS) is categorically mission-critical as neither of the primary payloads would be able to be sufficiently operated without achieving the desired orientation and stability.

Background and motivation

The past decade has truly been a golden age for the CubeSat standard with more than a thousand satellites launched and counting. However, the success rates of university-developed CubeSat nanosatellites are near-catastrophic, as only a third of the nearly 300 satellites launched in the past two decades by universities, high schools and other hobbyists have achieved their mission or are still in progress [1]. While not the biggest cause of failure overall, difficulties and partial or complete failures of nanosatellite missions can still often be accredited to failures in or at least the uncooperativeness of the Attitude Determination and Control Subsystem (ADCS) due to lack of qualification and acceptance testing, either in a temporal sense or by not following best practice standards. More recent examples of ADCS-related difficulties are the Aalto-1 and PicSat [2] nanosatellites, both of which are 3U sized CubeSats similar to ESTCube-2 that experienced serious issues with their attitude control and therefore failed to meet some or all of their mission objectives. ESTCube-1 also suffered through a partial mission failure due to its ADCS system lacking strength to overcome residual magnetisation of some of its structural components, and a severely time-restricted testing campaign.

With that in mind and in order to ensure the best odds of achieving primary mission success for ESTCube-2, the mission critical attitude determination and control components are subjected to nearly half a year of crucial subsystem specific and later integrated testing, something non-industry built CubeSats often lack funds or time for [3]. This will be in accordance with the active list of standards from the European Cooperation for Space Standardization (ECSS) [4]. This thesis is the body of text surrounding that testing campaign conducted by the author and serves as the documentation of the test results necessary for internal Quality Control procedures and setting the path for AOCS documentation to be presented to the launch provider.

The author has been the acting team lead for the AOCS subsystem of ESTCube-2 for the past two years and will continue work on the subsystem and the whole satellite as CEO of the Estonia Student Satellite Foundation until the primary mission is achieved. The author has recently published an article in the leading aerospace journal Acta Astronautica in collaboration with the ESTCube-2 and Finnish FORESAIL-1 satellite teams describing respective mission architectures and satellites [5].

Thesis objectives and structure

The presented thesis is a culmination of the more-than-four-years-long design process of the attitude control systems for the ESTCube-2 satellite. As such, it will build upon multiple past theses, for which it will serve as a final confirmation of the design choices. The thesis will not cover the higher-lever attitude determination and control software and algorithms, nor the sensor and actuator selection process, nor AOCS-specific electronics and hardware development, which have been presented in various past theses.

The thesis will firstly document the testing process of the chosen sensor (*Sun sensors, accelerometers, gyroscopes and magnetometers*) and actuator (*reaction wheels, magnetorquers and cold gas propulsion*) hardware for the engineering model. In the second part, the author will give an overview of the analysis of the testing and calibration data. In the last part of the thesis, the ability of the attitude control system to fulfil set mission requirements is evaluated and a set of guidelines is provided for the necessary final calibration of the ESTCube-2 flight model's space-bound hardware.

The units used in this thesis are standard SI, unless specifically noted otherwise.

Chapter 1
Testing Process

Overview

The difficulty of preparing for the harsh environment of outer space, where solar and cosmic radiation is bound to fry electronics, components are in danger of overheating or freezing due to extreme thermal fluctuations perhaps once every single orbit, or around 90 minutes, and while everything is in complete vacuum and hundreds of kilometres away, zooming around 8 km/s, and with no debugging pit-stops allowed, is one of the major reasons for the low success rate and a low overall life expectancy of small satellites, especially amongst the private sector, e.g. hobbyists, universities etc. [1]. This inherent danger can be mitigated by following a strict and thorough testing, qualification and acceptance process. As smaller companies and other non-industry based projects usually run on limited funding or a limited workforce, the immense backlog of sufficient qualification testing work-hours is usually a big constraint on the quality of the testing procedures.

This thesis covers much of the done and future in-house testing of AOCS hardware, especially sensors for our Engineering Model (EM) qualification following our own requirements. This is still the first step in the qualification and acceptance testing required for the launch of a satellite using Arianespace's Vega-C rocket with the European Space Agency's (ESA) In-Orbit Demonstration/Validation (IOD/IOV) programme [6]. To that extent, the Flight Model (FM) testing for ESTCube-2 will follow the industry standards set by the European Cooperation for Space Standardization, such as the ECSS-E-ST-10-03C for testing standards [7] and requirements and ECSS-E-ST-60-30C for AOCS requirements [8], and the clauses relevant to CubeSats on IOD missions [9]. As a low-budget small CubeSat manufacturer with an IOD mission built upon many published and upcoming scientific articles, ESTCube-2 shall fall

under the “Proto-Flight testing” category for ECSS standards, meaning we focus on qualification and acceptance tests on our only FM. This will be further discussed in Chapter 3 – AOCS Evaluation and Flight Model Calibration.

This chapter gives an overview of the testing equipment used, along with descriptions of test setups and any other relevant procedural information. As this thesis covers the documentation of a broad spectrum of different sensor and actuator tests throughout the whole testing campaign, the chapter first covers general testing equipment specifications before getting into more detailed EM sensor and actuator test setups. Tests that are considered part of the Engineering Model qualification testing are presented in this chapter, while qualification and acceptance testing for the Flight Model are presented in Chapter 3. The compiled requirements for the AOCS subsystem are collected and presented in Appendix A. The entire AOCS testing and calibration plan for the Engineering and Flight Models is presented in Appendix B. The individual tests conducted are also documented in the testing protocols which can be found in Appendix C at the end of this thesis. Short descriptions of the sensors and actuators can be found at the beginning of Sections 1.2 and 1.3 respectively, where the purpose of various sensors and tests is established.

1.1 Testing equipment and setup

The testing for the AOCS subsystem in the scope of this thesis was conducted in various laboratories of Tartu Observatory – Electronics Laboratory, Optics Laboratory and Clean Room –, and in the Institute of Physics – ‘*DigiLab*’ etc. The tests were accomplished with the help and supervision of the laboratory personnel of the Tartu Observatory and with the aid and know-how of the members of ESTCube-2 AOCS, On-Board Computer Subsystem (OBCS) and other teams.

1.1.1 Solar Simulator

Testing the satellite’s Sun sensors requires a light source that can viably simulate the solar irradiance spectrum outside the Earth’s atmosphere. For that and other optics and solar panel testing purposes, Tartu Observatory has acquired a modified SS150AAA Solar Simulator depicted performing a test in Figure 1.1. The modifications include a setting for no atmospheric effects, relevant for any space applications.

Feature	Specification
Lamp Type	Xenon Short Arc
Lamp Power	1000 W
Air Mass	AM0[1] / AM1 / AM1.5
Spectral Range	250 nm – 2200 nm
Spectral Match (to all intervals)	± 25% or better

Table 1.1: Photo Emission Tech., Inc. Solar Simulator Model SS150AAA datasheet [10]

Figure 1.1: SS150AAA Solar Simulator

The solar simulator is still the best way for us to test our Sun sensors and solar cells with their satellite-critical maximum power point tracking operations in ranges most closely resembling final mission conditions, and it was used widely during the prototyping phase in AOCS, especially as there were weekly tests to determine the best thickness of coating for the Sun

[1] Modification compared to the original datasheet.

sensors and to acquire a ballpark range for the expected field of view. This prototyping process is covered in Section 1.2.1.1. under Sun sensor design modifications.

1.1.2 The thermal vacuum and vacuum chambers

Tartu Observatory has an ALTA custom-built thermal vacuum chamber (Figure 1.2), which will be used for complete thermal vacuum testing the whole satellite system during flight model testing campaign. Each subsystem might be separately subjected to high vacuum using the chamber but will ultimately forego full thermal vacuum testing. This will be the case for multiple AOCS sensors and actuators that have not been subjected to high vacuum already during the manufacturing process, most specifically the Microelectromechanical (MEMS) Inertial Measurement Unit (IMU) sensors – gyroscopes, magnetometers and accelerometers. The manufacturing process of vacuum-coating the Sun sensors and out-gassing the epoxy-bound magnetorquers, as well as using industry built and space-grade Reaction Wheels (RWs) and the Cold Gas Propulsion (CGP) system allows us to forego the small-scale vacuum tests on those systems.

Feature	Specification
Test space volume, approx.	220 L
Ultimate pressure	$\leq 5 \cdot 10^{-7}$ mbar
Total leak rate	$\leq 1.4 \cdot 10^{-4}$ mbar·dm^3·s^{-1}
Performance for temp. tests, min/max	– 40 °C / +250 °C
Temp. gradient	Up to 5 °C/min

Table 1.2: Features from ALTA Thermal Vacuum System datasheet [11]

Along with the certified and space-grade thermal vacuum chamber, an older simple vacuum chamber is used for prototyping and tests. Besides the logarithmic mV-to-Pa calibration curve comparing millivolts of a vacuum chamber internal sensor to pascals of pressure inside the dome, not much is known about the model or other characteristics of the chamber. The glass dome of the vacuum chamber means that it is easy to connect with the sensors inside the chamber wirelessly, as opposed to the thick metal ALTA high-vacuum chamber, making it the ideal quick demonstration for vacuum related prototyping, degassing and testing.

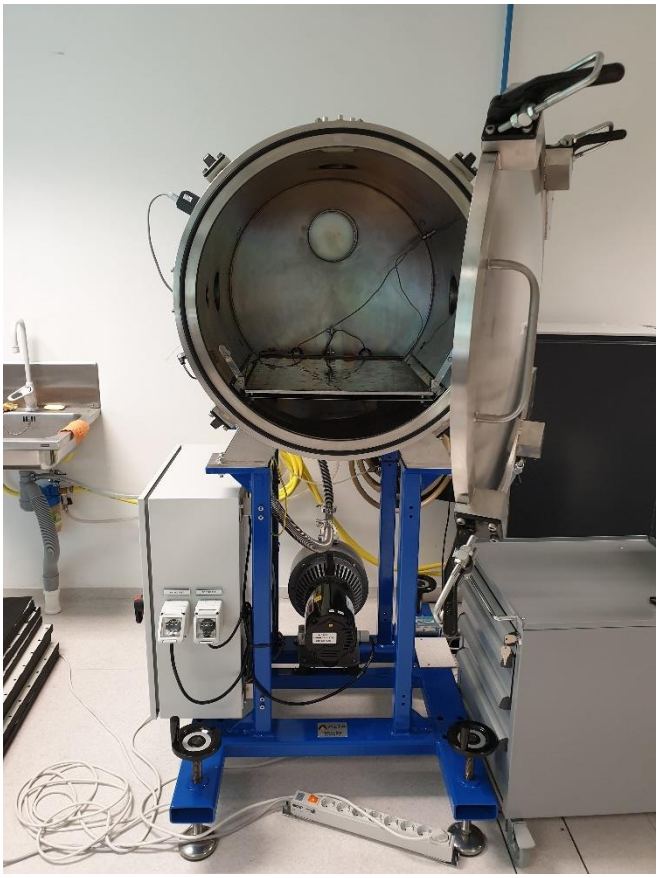

Figure 1.2: Thermal vacuum chamber

1.1.3 Temperature and climate test chamber

Many of the preliminary thermal tests can be done in a temperature chamber instead of the more advanced thermal vacuum chamber, in which the full-scale tests could take several weeks per subsystem as the temperature of the subsystem can only reach equilibrium with the ambient one via radiation. The temperature and climate test chamber in use at the Observatory is the Weiss Technik model WKL 64/40, shown on Figure 1.3.

Feature	Specification
Test space volume, approx.	64 L
Performance for temp. tests, min/max	– 40 °C / +180 °C
Temp. consistency in time	max. ±1.0 °C
Temp. homogeneity in space	max. ±2.0 °C

Table 1.3: Weiss Technik Temperature and Climate Test Chamber WKL 64/40 datasheet [12]

Figure 1.3: Weiss WKL 64/40 Temperature chamber

Flight results of CubeSat missions such as COMPASS-1 and ESTCube-1 have shown temperatures ranging from -5 °C to +25 °C on the subsystem boards and from -20 °C to +40 °C on the side panels behind sun sensors (COMPASS-1) [13], while ESTCube-1 reported temperatures ranging from 0 °C to +30 °C [14]. The thermal chamber is thus able to test the working temperature range set for EC-2 mission of -20 °C to +40 °C and demonstrate thermal withstand ability of -40 °C to +60 °C.

1.1.4 Rotating bench

Various types and configurations of rotating benches are one of the most commonplace pieces of equipment when dealing with sensor and actuator testing. Free running rotating benches are used to test the functionality of satellite actuators such as reaction wheels and thrusters while controlled rotating benches can be used for sensors, most specifically gyroscopes. Controlled rotating benches can also be used to aid in the calibration of accelerometers as they can be subjected to varying levels of centripetal acceleration. At small accelerations, speeds and bench sizes, this is however greatly disturbed by the constant gravitational acceleration. Rotating

bench might also be used for the calibration of magnetometers to get a reading of the same magnetic field using all the different octants of the sensor's coordinate system.

Gyroscopes are one of the few sensors in an IMU which can be sufficiently simply calibrated on the ground, since they are not hindered by the existing gravitational acceleration or magnetic field, both of which have quite an enormous magnitude considering space applications. As the gyroscopes also aid greatly in the attitude prediction step of the Kalman filter, it was paramount for the AOCS team to construct a small and compact rotating bench, that could also be operated in the thermal and possibly inside the vacuum chamber as well. Due to primary mission requirements the rotating bench should be able to reach similar speeds as envisioned in the mission architecture, e.g. up to 360 °/s and more and revolve at that speed at a stable speed.

Such a rotating bench (Figure 1.4) was built by the AOCS team under the author's supervision over the course of summer 2019 using available materials. The main structure of the bench originates from a duplex filter tuning apparatus in an UHF radio station, which used the smooth rotation to change the length of the filter's resonator. The rotating bench itself sits atop a simple adjustable table and a large flywheel is fitted on top of the rotator. The adjustable table allows for it to undergo a levelling process before every test session as any tilt in the axis of rotation from the direction of gravity along with a possible inaccuracy in the centeredness of the flywheel with regards to the axis of rotation and thus the inertia matrix of the whole rotating bench will cause an avoidable periodic disturbance in the angular velocity of the system.

A further two systems were developed for the rotating bench by the author: the tachometer and driver systems. The tachometer giving us the angular velocity measurement consists of a Photologic OBP461T11 optical switch, a separate 3D-printed encoder gear with 270 cogs fitted around the rotating bench and an Arduino Nano to calculate the angular velocity with the elapsed time given out by the passing of cogs between optical switch. The 270-cog wheel was chosen after test prints showed a sharp decrease in quality for wheels up to 360 cogs. This approach was taken over a specialised rotary encoder for the ultra-low cost, simplicity and ease of integration to our bench. To drive the rotating bench, a FIT0441 brushless DC motor with a built-in motor driver was acquired. The electric motor drives the rotating bench using a rubber transmission belt and draws power direct from a power supply with the speeds controlled by PWM signals from the same Arduino Nano.

Both the jerk of the accelerating and decelerating electric motor, any effects from torque ripple as well as the accuracy of the 3D-printed cogs are major sources of noise in the system and

have to be accounted for in subsequent calibration processes. The dimensional accuracy of the 3D printer can be found from the datasheet [15] and an inaccuracy of the print can be estimated. The use of a rubber band transmission and separating the sensors from the rotating bench using with correct materials has a strong dampening effect on the vibrations and noise generation. Compared to the uncertainties from the aforementioned sources, the author considers the uncertainties from possible time lag in Arduino internal clock and data transfer to be several orders of magnitude lesser and can be therefore disregarded in the first approximation.

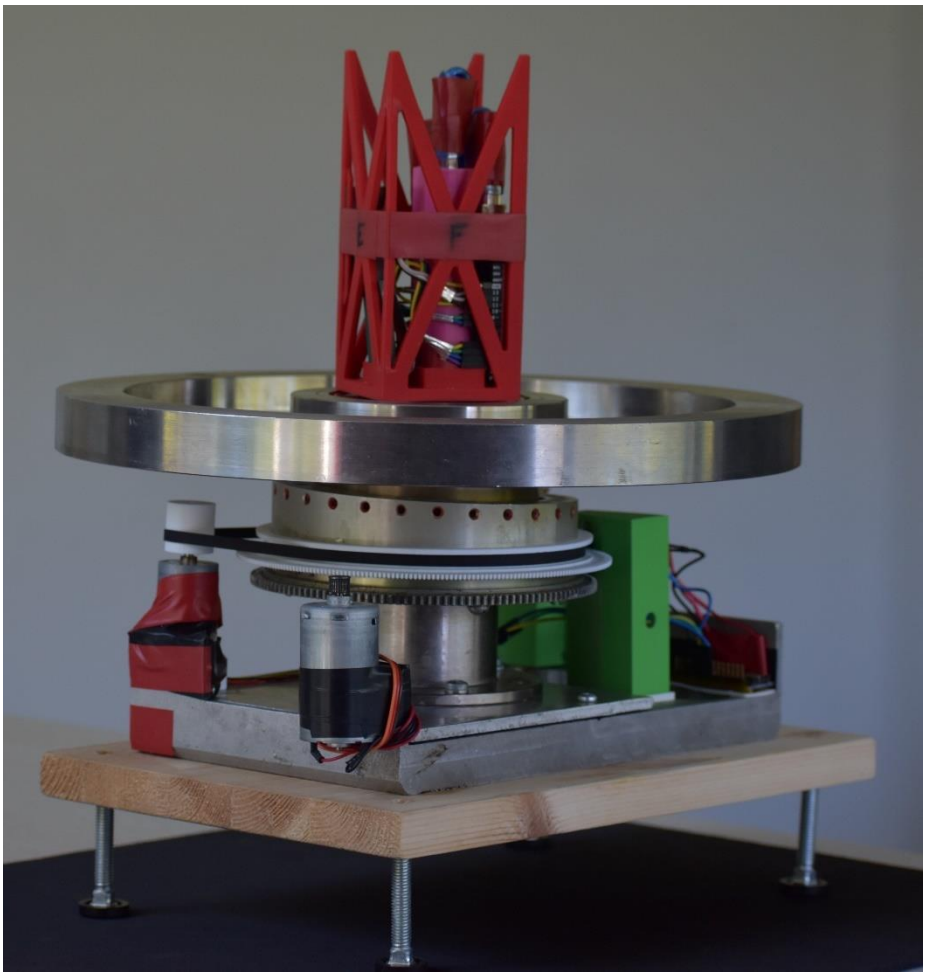

Figure 1.4: Rotating bench developed for EC-2. The bench is equipped with 3 motors, which were tested to find the best. The Arduino Nano is visible on the lower right side. The white gear has 270 cogs, which are read by the optical switch held up by the green frame.

Estimation for the combined uncertainty of the angular velocity of the rotating bench at higher speeds was completed for the prior 90-cog encoder wheel:

$$U^C = 0.0025 \cdot \omega + 0.039\,^\circ \cdot s^{-1}, \quad where\ \omega > 30\,^\circ \cdot s^{-1} \tag{1}$$

An in-depth analysis of the noise and uncertainties originating from the rotating bench can be found in Appendix C.1, but this is subject to be superseded during the Flight Model calibration phase as the AOCS team has acquired a 10,000-step rotary encoder to log the speeds of the rotating bench.

1.1.4 Sun sensor testing bench setup

To map out and measure the intensities for the entire required 90-by-90-degree or larger FoV of the Sun sensors, a two-axis adjustable test setup was prepared in the Optics laboratory in Tartu Observatory. Test setup consists of two optical grade motorised rotating tables model no. MOR-100-30-A from Optics Focus Instruments Co., Ltd., which have been connected by an U-shaped connector (*Figure 1.5*). The first of the rotary stages sits atop the optical bench and turns the connector frame itself while the other turns a rod with the Sun sensor PCB fixed onto it. The rotating tables are controlled remotely by a controller, model no. 7SC304 from Beijing 7-Star Optical Instruments Co., Ltd. This in turn can be accessed via an USB-serial port and thus automated.

The size and setup of two-dimensional testing does not allow the use of the vertically mounted Solar Simulator and an alternate sufficiently powerful light source must be used. This will cause a discrepancy in the response of the Sun sensor, which will need to be accounted for outer space operation. A sufficient light source was found to be an Oriel GmbH.-made 450 W Xenon Arc lamp, model no. 66923 and powered by their 69920-model power supply. The spectral irradiance from the arc lamp can be slightly tuned by adjusting the collinearity of the beam. This slight deviation from the collimation will not exceed 1 degree. The justification for the tuning is the dispersion of a similar magnitude of Solar light rays and the fact that it allows us to limit overexposure of the Sun sensor array and get an accurate reading of the intensities across the whole solid angle in question, while direct light from the Sun would saturate the digital sensor in its centre region.

The test setup will be aligned using a laser to have the tested sensor centered in regard to the light source under all planned rotations. Both of the rotating tables as well as the Sun sensor will be connected to a computer, which is programmed to scan the Sun sensor through the required orientations and log the respective digital sensor responses, of which maximum values are used for the correlation function.

Feature	Specification
Arc lamp housing model	66923, Oriel GmbH
Arc lamp type, nominal power.	Xenon Arc, 450 W
Arc lamp output beam width	69 mm collimated
Motorised rotary stage model	MOR-100-30-A
Motorised rotary stage resolution	0.00125°

Table 1.4: Sun sensor test setup specifications.

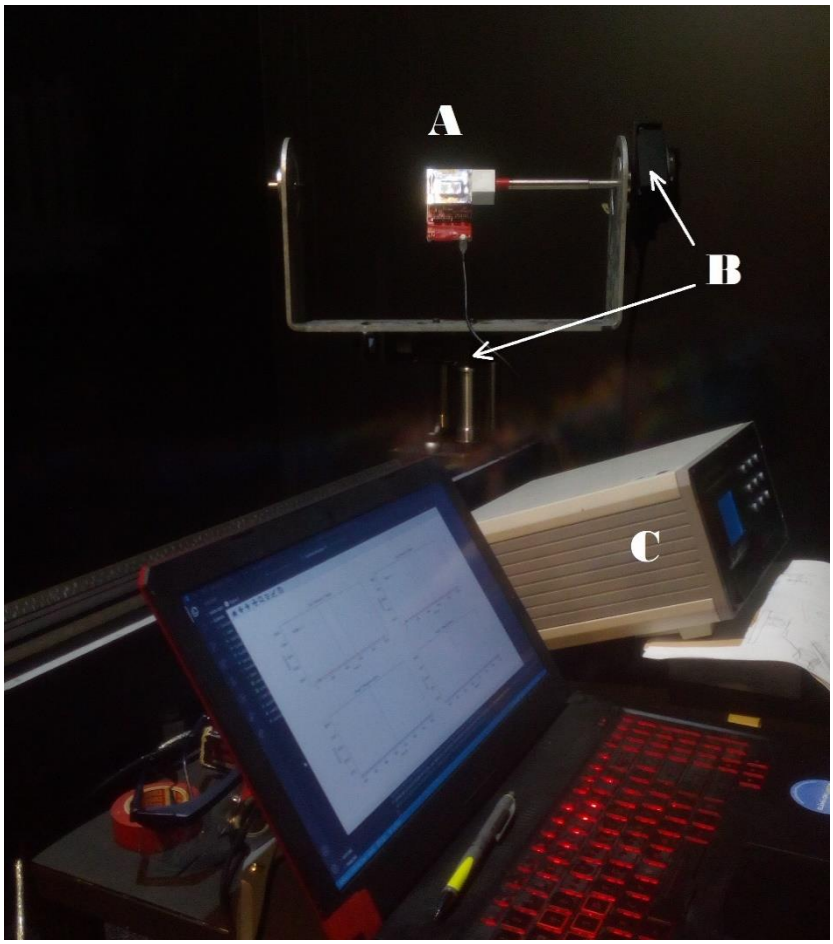

Figure 1.5: Sun Sensor test setup in the optics lab of Tartu Observatory. A – Sun sensor and fixture. B – Two stepper rotary stages. C - Controller

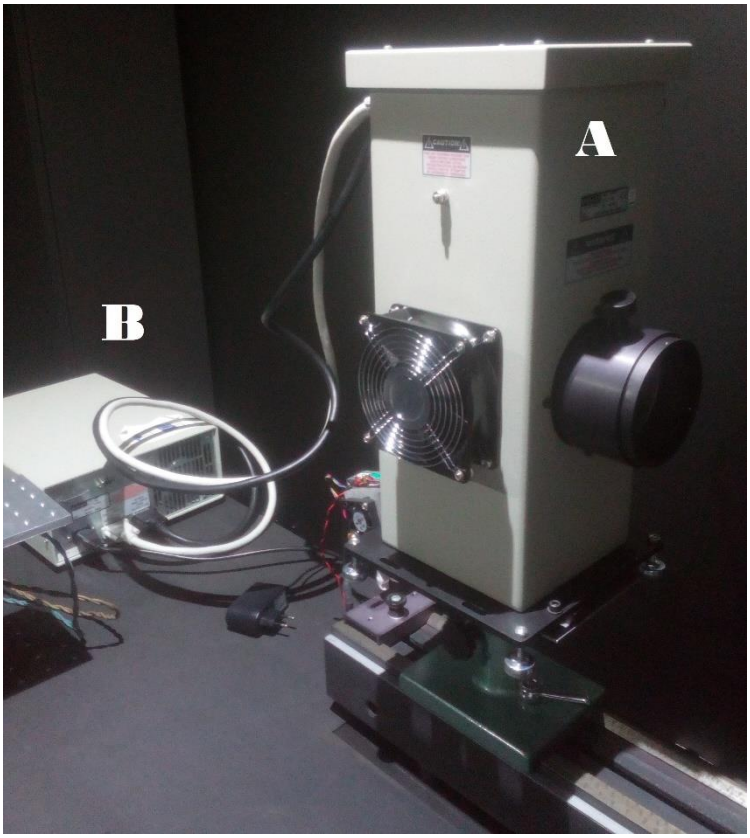

Figure 1.6: Sun sensor test setup light source.
A – 450 W Xenon Arc Lamp. B – Power supply.

1.2 Sensor tests

The following section will give a short overview of the Commercial Of-the-Shelf (COTS) sensors themselves and their qualification and calibration testing procedures. Some of the tests in the scope of AOCS testing campaign may have been performed in the framework of other theses, such as the selection and basic functionality testing of the IMU sensors by Madis Kaspar Nigol [16] or the Sun sensors by Aleksander Parelo [17]. These preliminary tests are considered necessary prerequisites to the qualification testing of ESTCube-2's sensors for thermal, vacuum, shock and vibrational durability and are thus included in the AOCS testing plan, presented in full in Appendix B. The testing and calibration presented in this thesis will mostly cover engineering model qualification and functionality testing, with a perspective on subsequent flight model qualifications.

Throughout the development of ESTCube-2, and especially the past couple of years, the focus of the AOCS team under the authors lead has been on the Sun sensors and magnetometers, as they are considered perhaps the most essential of the attitude determination sensors in the satellite, allowing us to solve Wahba's problem, meaning determine our attitude unambiguously using two independent vectors in time and space. To that extent, every side of the satellite has its own set of Sun sensors and magnetometers to have sufficient redundancy at this most fundamental level of AOCS. The Sun sensors used on EC-2 are Hamamatsu S9226 series CMOS 1x1024 pixel, linear image sensors [18] and the magnetic sensors are low-power, high performance LIS3MDL 3-axis magnetometers [19]. These are backed up by multiple redundant BMG160 3-axis gyroscopes [20] that allow the satellite's Unscented Kalman Filter to refine its attitude estimation and propagation through time. This important sensor trio is joined by the FXOS8700CQ 3-axis accelerometers [21], mostly for side panels deployment and Cold Gas Propulsion module operation verification.

General note on thermal testing: the data collection for working range tests and power-down mode for durability tests will be 60 minutes in duration, as the time to complete one orbit around the Earth at a Sun-synchronous 500 km LEO is about 90 minutes, meaning that the time spent in eclipse (behind Earth) might vary from 0 to about 30 minutes, depending on the launch profile. The 60-minute stress test amply covers the max envisioned time spent in eclipse and is around the amount of time we configure our satellite to spend in direct sunlight.

1.2.1 Sun sensor tests

While the Sun sensors themselves have been replaced with digital ones and with that some of the structural components have changed, the idea of ESTCube's two-axis Sun sensors remains essentially the same as on the first satellite, ESTcube-1. Although the development of the Sun sensors for ESTCube-2 has been partly covered by a previous specific thesis, Aleksander Parelo's "*Development of ESTCube-2 side panels*" [17], some additional modifications to the original design will also be introduced and documented in the presented thesis. Rest of the sub-section will cover the main qualification tests done and ongoing on the Sun sensors.

1.2.1.1 Sun sensor design modifications

One of the large drawbacks of the switch from position sensitive detectors to a CMOS linear digital image sensor relates to the sensitivity and saturation issues of the latter. These can be managed to some extent with clocking and software, but in order to be

fully functional as a single-slit Sun sensor in outer space, a way of reducing incident light is required, either in form of filtering or a reflective coating. This is the conclusion arrived to by Aleksander Parelo in his 2018 thesis, which examined the permittivity of different filters such as the UFS-1, but further prototyping of the sensor was deemed necessary.

Due to dimensional constraints on the satellite structure, which follows the CubeSat standard along with the dispensing mechanism for the satellite, the option to filter out excessive levels of Solar radiation was later discarded and a reflective film coating for the sensors was instead pursued by the team. The reflective coating prototyping and selection was done through the winter and spring of 2019/2020 by the author with the help of prof. Aarne Kasikov from the Thin Film Technology Laboratory of the University of Tartu. Multiple configurations of evaporated titanium and gold layer depositions were tested with the final selection on pure Ti coating.

The following is a translation of the notes received from the Thin Film Technology department on the experiment: “The deposition uses a vacuum-vaporisation chamber VS-17 at $(1...4)\cdot10^{-4}$ Pa with electron beam vaporisation of the source material, previously melted and thawed pieces of titanium placed inside a C-crucible. The time of the vaporisation and thus the thickness of the deposited layer is controlled by a quartz oscillator. Speed of vaporisation is 0,15 nm/s to 0,25 nm/s and throughout the experiment, the internal pressure of the chamber remains at $(1...4)\cdot10^{-4}$ mbar. The results for the chosen sensor coating deposition thickness were measured by X-ray fluorescence calibration to be approximately 155 nm. There was no effort made to optimise the vaporisation conditions.”

The frame to hold the sensors was manufactured by the author and milled out of a polycarbonate type that did not cause noticeable outgassing issues for the chamber. Prior to the titanium deposition, the sensors were cleaned with either an abrasive or with a strong solvent. Both were finally rinsed using ethanol. As no flaking or other issues have appeared with either of the choices in the duration of working with the coated sensors, the difference will be disregarded for the duration ESTCube-2 integration and mission, but further testing of both should ensue, should a similar linear image sensor approach be undertaken with similar saturation issues.

The thickness of approximately 155 nm was arrived to by numerous trial and error tests and subsequent refinements if the initial guess. This thickness aims to optimise the overall field of view along with the sharpness of the peak seen by the sensor, which unfortunately causes the signal to saturate and plateau in the centre region on the sensor given an emphasis on the maximal field of view.

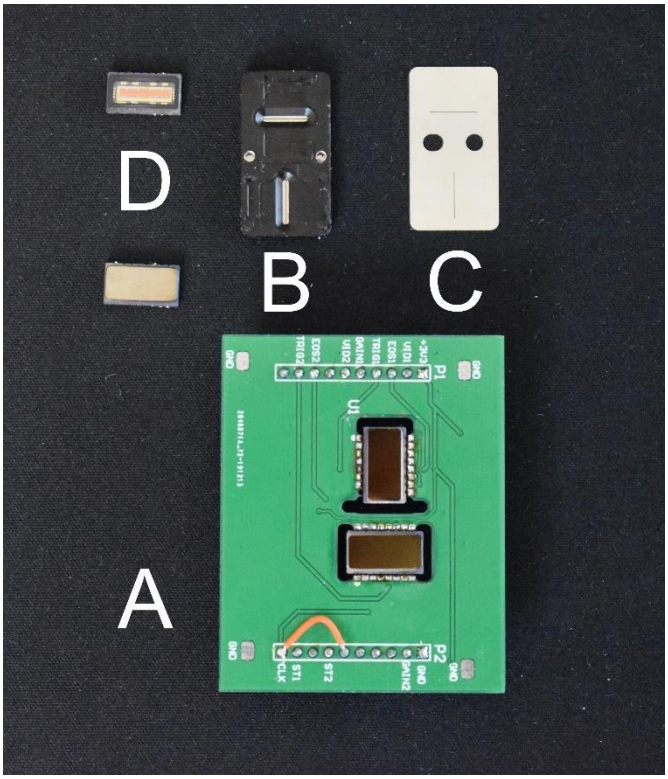

Figure 1.7: Sun Sensor components: A – Sun sensor PCB with two engineering model titanium-coated sensors. B – anodised aluminium mask underside. C – 30 μm stainless-steel cover with 100 μm slits. D – a coated prototype sensor and an original sensor.

Other changes to the previous design can be found with the mask composing of two parts: the anodised aluminium body and the 30 μm thick stainless-steel cover. The slit of the mask body was narrowed, and the underside bevelled to give more support and contact surface with the thin mask cover on top. This change was done to avoid potential damage or deformation of the unsupported steel edges from launch vibrations or during handling and integration. This was shown to be the case during early prototyping, where, while integrating the mask to the sensor board, the edges of the stainless-steel mask cover were deformed and consequently the field of view obscured.

The slit of the sun sensor was chosen by the author to be 100 μm following tests with 125, 100 and 75 μm slits. This also aimed to maximise the useful field of view while minimising oversaturation of the sensor. The inside of the stainless-steel mask cover will be painted black to minimise and disperse internal reflections from the titanium coating at small angles of incidence, where the reflections would bounce multiple times between the reflective surfaces inside the sensor. The final product is shown disassembled on Figure 1.7.

1.2.1.2 Sun sensor two axis intensity mapping

The previous, 2013 ESTCube-1 mission results gave us a good insight to what needs to be improved about our testing procedures. One of such lessons learned was the failure to accomplish true in-orbit verification, refinement and recalibration of our Sun sensors because the prelaunch calibrations of the sensors were done in a single dimension only with expectation that the sensor response linearity is preserved off-axis [22][23]. This expectation proved to be void and the use of Sun sensors was highly challenged due to aforementioned non-linearity but also by a drift in sensor reference voltage. To this extent the Sun sensor two axis testing bench was set up to correctly map out the intensity change over the whole required field of view, at least ±45 ° in both directions while a bigger range would be preferred to have the sensors vision overlap and avoid blind spots for the attitude determination.

The test will be focused on a single sensor of the two on each sensor board, as each one is more or less identical to the rest in theory. Differences may appear in soldering accuracy, mask placement, as well as differences in coating thickness. This means the same tests will be done on a random sample of engineering model sensors to account for any possible discrepancies.

The automated test will scan over the sensor field of view from -60 ° to +60 ° in two axes in increments of 3 °. In each position, the Sun sensor will log 10 images worth of data before moving on to a new position. The preliminary results of this test are analysed in Chapter 2, Section 2.1.5. While the data might look promising, care must be taken with consideration of the rotation angle calculation for the sensor coordinate frame, or the theoretical angle of incident light in the experiment. It is currently under consideration if the testing setup configuration needs to or even can be changed to avoid complications with a type of spherical projection calculations relevant to ours.

1.2.1.3 Sun sensor thermal functionality tests

There are two types of thermal functionality tests that the Sun sensors will be subjected to along with the IMU sensors: ones testing the working range and the others testing the survivability of the sensor in thermal extremes. Both of the tests use the Weiss WKL thermal chamber in Tartu Observatory.

Working range test will demonstrate that the Sun sensor encounters no issues being powered on for an hour at -20 °C and at +40 °C. The beginning of the test will wait until the temperatures have stabilised within ±1 °C, which is the sensitivity of the internal temperature sensor in charge of the feedback loop. The test will use uncoated sensors as it is easy to verify the continued functionality of the sensor even with ambient lighting or a flashlight. The Sun sensors will not be stress tested with constant data logging throughout the test but intermittently the data is logged, and functionality is confirmed. This test was passed, and no issues were detected, no further analysis deemed necessary. This test was done in conjunction with the IMU sensors and the test protocol is presented at Appendix C.2.

The sensors were also tested for their capability to withstand thermal range extremes. The thermal chamber was heated up to +60 °C and the Sun sensor board in power-down mode was inserted. Time was given for temperatures to equalise and the sensor was left there for 60 minutes. After this, the sensor was cooled down to room temperature and its continued functionality was verified. The test was repeated at the other required thermal extreme at -40 °C. The sensor showed no permanent defects and no further analysis was deemed necessary. This test was done in conjunction with the IMU sensors and the test protocol is presented at appendix C.3.

1.2.2 IMU sensor tests

The Inertial Measurement Unit consisting of gyroscopes, magnetometers and accelerometers is the industry standard for a large part of technology, from mobile phones to anything robotic or automated. The first section will present the 3D-printed remote sensor testing frame, that was used to log data from the IMU sensors. The rest of this section will cover the necessary qualification and calibration tests to bring the affordable COTS components up to the performance standards we require for a successful space mission. As the IMU sensors are

mounted on a common AOCS sensors PCB, many of the tests were ran for the whole sensor group together, such as most thermal and vacuum testing.

1.2.2.1 3D-printed IMU sensor testing frame

It became apparent early on in the development of AOCS sensors and algorithms, that the final integration with OBCS will take time and that testing and calibrating the sensors should happen sooner. Calibration of the 3-axis MEMS sensors is also a very coordinate-system-and-rotation based process, meaning that the orientations of the sensors need to be fixed, achievable within a couple of degrees and unmistakably designated, to complete the calibration process. Another constraint on the IMU sensor testing setup was the requirement to log data in real time and wirelessly, which immediately caused the addition of a HC-05 Bluetooth COM device and a small battery pack. The need to log data remotely was first discussed due to the rotating bench but ended up being necessary to conduct both thermal and vacuum testing without a large effort of connecting everything through specialised pin connectors.

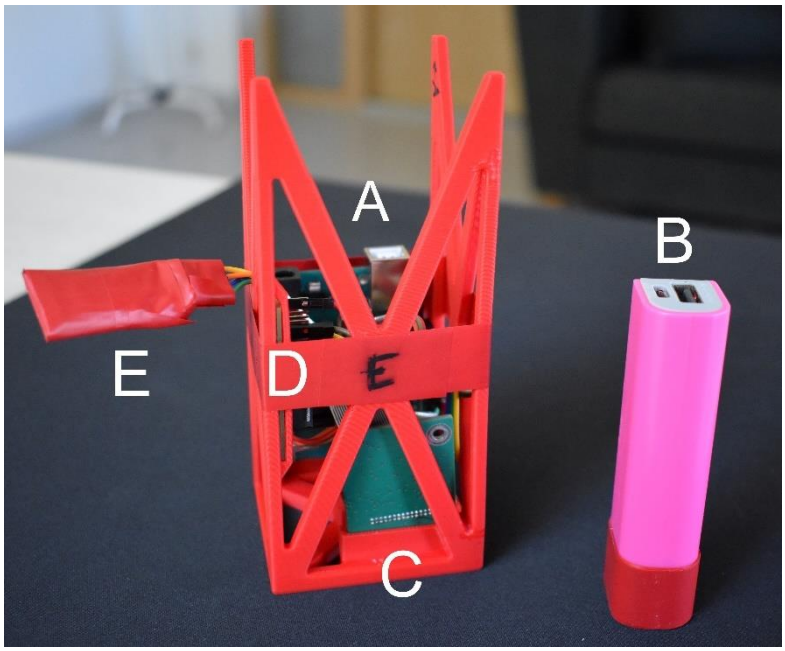

Figure 1.8: 3D-printed IMU sensor testing frame. A – Arduino Uno. B – Battery pack. C – IMU sensor board. D – Adapter board. E – HC-05 Bluetooth device. Note that each side was designated a letter similar to the "E" written on the side for data management.

The sensor board, which was originally integrated to the OBC prototype board, was rewired to an Arduino Uno board using an adapter PCB and everything was fit tightly inside a 60 mm by 60 mm by 140 mm 3D-printed frame, depicted on Figure 1.8 and designed under author's requests and oversight. The sensors on the board follow a Serial-Peripheral Interface (SPI) architecture, which was another important lesson learned from the EC-1 mission [22, p.17], that used the Inter-Integrated Circuit (I2C) bus, which ended up causing data corruption and sensor communication issues. The mass of the total portable IMU sensor testing pack is 181.6 grams. The required Arduino software for remote data gathering and transmission was written by the author.

The 3D-printed sensor testing frame had a total of 14 different orientations that were under consideration and logged for data calibration. These are the 6 facets of the parallelepiped (from A-F), and each of the 8 corners (bottom K-M and top P-S). Logging data on a rotating bench in each of these 14 orientations is visible on Figure 2.5 in Chapter 2. A special base with a triangular cutout was made to house the testing frame in the 8 corner positions.

1.2.2.2 Common IMU sensor tests

Thermal withstand and functionality testing was done in conjunction with the other IMU sensors and the Sun sensors with no special conditions for any of the sensors. They are presented in Appendix C.2 and C.3 respectively.

Low- and high-vacuum testing was done in conjunction with the other IMU sensors with no special conditions for any of the sensors. Results from Low Vacuum test using the older vacuum chamber are presented briefly in Chapter 2. High vacuum testing was done with the sensors at standby, subjected to 60 minutes of pressures around $1 \cdot 10^{-5}$ Pa. Sensor data was logged before and after the test, bus the data analysis is still ongoing. No permanent functional problems were encountered during this test.

1.2.2.3 Gyroscope calibration

Biggest obstacle to tackle for gyroscope measurement calibration was the chain of problems operating the rotating bench. In order to calibrate the gyroscopes, a steady and adjustable angular velocity must be achieved to calibrate the satellite's gyroscopes in a very large range of speeds. This is governed by the science mission requirements on board ESTCube-2, which include both two large and high-resolution low-end visible

and near-infrared Earth-Observation Cameras requiring fine pointing and stability, and an experimental electric solar wind sail (E-Sail) experiment, requiring super-high angular velocities up to 360 °/s around a specified axis while preserving the fixed pointing capabilities of said axis.

As problems with the stability in rotation of the rotating bench did not cease, instead a time-sync approach was taken with the calibration of gyroscopes. This meant that in order to accurately match the data from the gyroscopes to the encoder data from the rotating bench, a master-device first had to time-sync both before the experiment could begin. This was achieved by modifications to the rotating bench encoder code as well as the sensor board code, both of which were to wait for a command sent by a computer logging the data before beginning data transmission. The initiation commands were sent in quick succession and the timestamp of receival was logged by the encoder and the sensor board. This was subtracted from the reading of their internal clock and added as a "synchronised" timestamp to the measurements sent to the master computer. The prototyping of this setup was done by the author and Robert Märk of the AOCS team over the summer of 2020 and the first results are presented as a gyroscope calibration data in Section 2.1.2. This testing was done on the low end of the velocity-spectrum, in finer steps from 0 °/s to 20 °/s, while the whole range should go up to 360 °/s in several larger steps.

The thermal calibration of the gyroscopes was done by fitting and levelling the rotating bench inside the Weiss WKL 64/40 thermal chamber at -20 °C, 0 °C, 20 °C and 40 °C. Temperature was measured with the internal sensor for closed-loop temperature control, which has an error range of ±1 °C. Data was only logged when the temperature had settled down to this range after each orientation change.

1.2.2.4 Magnetometer calibration

Magnetometer calibration for local use on Earth is inherently a simpler process than gyroscope calibration. This can be done hand-held and in under a minute, as is the case with recalibrating smart-phone IMU-s. Difficulties arise with the requirement to calibrate the magnetometers throughout their whole proposed range of field strengths encountered in 500 km SS-LEO, between 20 μT to 60 μT. While the setup for this sort

of a test is not a problem on its own using sufficiently large and calibrated Helmholtz coils, the problem arises from the magnetic disturbances by a multitude of metallic and electrical components in the vicinity of the test. The test could be done outdoors and relied upon the World Magnetic Model to calculate the near-exact theoretical magnetic field magnitude and heading in that location for the final results. This, however, will prohibit the necessary thermal calibration needed for space operations. The only option is to calibrate the magnetometers in the required range of field strengths at one temperature and then separately calibrate the magnetometers thermally in the presence of a single and distorted magnetic field due to the thermal chamber. These two results can then be interpolated and/or extrapolated in two dimensions (depending on the magnetic field strength inside the chamber) to arrive at the complete calibration parameters.

Magnetometer measurement calibration done in Chapter 2 only represents the proof-of-concept of our sensor calibration in the Earth's natural magnetic field. Since the magnetic field will also be distorted by the satellite FM, the final magnetometer calibration for the working range is scheduled to be completed then. While Tartu Observatory has access to Helmholtz coils built for the previous EC-1 mission, this calibration will take place in an accredited calibration company Kiwa Inspecta, that has all the right equipment and calibrated sensors on site to confirm the magnetic field our FM magnetometers will be subjected to.

This thesis will present the latter of the two separate calibrations, the thermal one, in Chapter 2. The thermal calibration data was collected through a similar procedure to the gyroscopes, at -20 °C, 0 °C, 20 °C and 40 °C, but at standstill, with the elimination of the rotating bench from the thermal chamber, to avoid unnecessary extra magnetic distortions. The other major distinction was that the thermal chamber was shut down for the period of data collection, to eliminate distortions due to electrical currents in the system. The chamber was restarted as often as necessary to keep the temperature in the ±1 °C error range.

1.2.2.5 Accelerometer calibration

Calibrating accelerometers poses the same class of obstacle as magnetometers – it's incredibly simple at ground value, even for thermal calibration, but getting to micro-gravity ranges without highly specialised equipment is impossible. For a full calibration

on Earth, one would have to devise a variable-speed revolving low-pressure drop test at different temperatures to collect data on the full calibration parameters without large amounts of inter- and extrapolation of results.

As with the magnetometers, the approach taken by the author is calibration in a fixed gravitational field strength but complete the full thermal calibration. The data for these tests is presented in Chapter 2, Section 2.1.4.

1.3 Actuator tests

ESTCube-2 is equipped with multiple sets of actuators, making it rather uniquely capable for a nanosatellite of its class, once again a requirement due to highly specialised science experiments and future prospects of a flight beyond low Earth orbit, to the Moon, which would losing the viability of magnetorquers. The other actuators are a set of three Reaction Wheels (RWs) model RW210.15 from Hyperion Technologies B.V. [24] and a Cold Gas Propulsion (CGP) module NanoProp CGP3 from GOMspace [25]. In-orbit testing of these attitude control systems along with our AOCS algorithms is vital to ensure the success for EC-2 primary missions in orbit, as well as for achieving the necessary confidence for future missions without the ‘safety net’ of the magnetorquers. This was investigated by the author and Robert Märk of the AOCS team on a theoretical level as part of a paper on EC-2 and FORESAIL-1 missions overview that has been accepted to be published in an upcoming Acta Astronautica issue [5]. The work for the article included development of a physical free rotation simulation of the EC-2 satellite and simple RW and CGP control algorithms, that included detumbling, pointing, desaturation and spin-up of the satellite to achieve all of its science missions.

The magnetorquers are the absolute standard for CubeSats and other small satellites using an active ADCS system (as opposed to a passively pointing one, such as a permanent magnet or a gravity gradient module) for their simplicity, low cost and low mechanical requirements, and ESTCube-2 is equipped with a 3-axis set of magnetorquers, one seen on Figure 1.9.

Most of final actuator functionality, qualification and calibration testing will fall under the category of Flight Model testing and as such is presented in Chapter 3, Section 3.2.1 – Pre-launch Flight Model testing campaign. This is because the more technically complex and

expensive actuators are bought in only for the Flight Model, and these are already flight-proven and have certifiably passed the necessary qualification and acceptance testing for use on ESA-related satellites. This means we can and will skip most of our in-house testing of these actuators and focus on Flight Model integration and closed-loop control algorithm testing.

Figure 1.9: One of ESTCube-2 Flight Model elliptical magnetorquers for the long side. Tape protects the loose wire ends from breaking off.

1.3.1 Actuator functionality tests

Each of the actuators shall, however, have to pass preliminary functionality tests. This will give us the green light to continue with control algorithm development knowing that the actuators themselves behave nominally out-of-the-box.

Magnetorquer functionality testing is essentially tied to the coil driver electronics development, which was prototyped by Aleksander Parelo in 2017-2018 [17] and the work on Engineering Model version has been continued by Aleksandra Doroshenko since 2019. The coils themselves are a simple concept on paper, just some wire, that just ensuring current can pass through it is in a sense the functionality test. The changing magnetic field is easy to verify with just the IMU of a smart-phone and any free 3D-compass app. True testing of the coil parameters can start in

autumn upon the arrival of the coil driver electronics, which have passed review and have been ordered.

Reaction wheels have been subject to functionality testing and debugging since 2019, when the author of this paper began the acquisition of RWs from Hyperion Technologies and requested a sample wheel to be tested for the aforementioned reasons – functionality testing and control algorithms development. Figure 1.10 shows the Hyperion RW210.15 testing wheel mounted inside the mock-up of ESTCube-2 bus, prepared for a sensor noise test while running the reaction wheels.

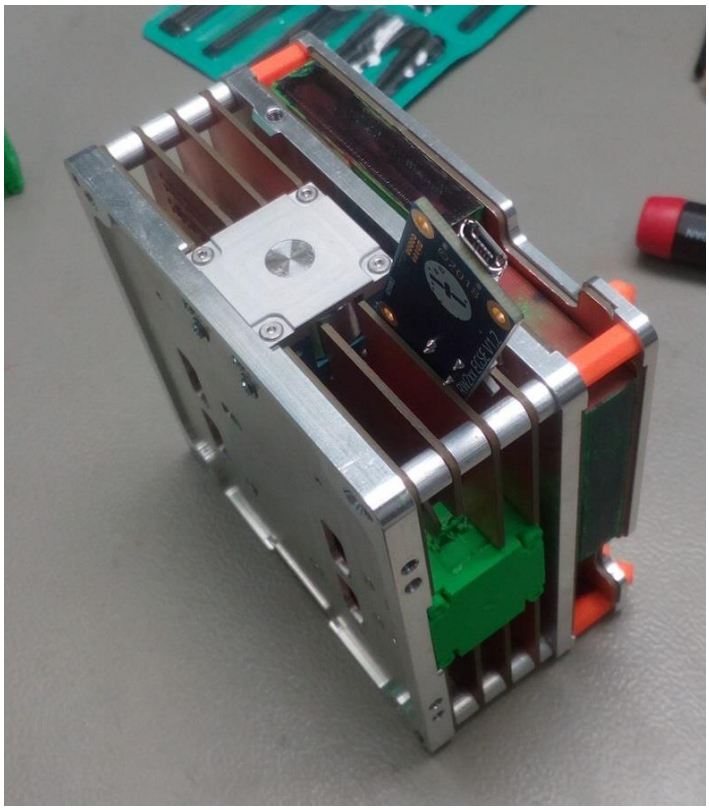

Figure 1.10: Hyperion Technologies RW210.15 mounted onto the EC-2 bus mock-up. Also visible is the provided Electrical Ground Support Equipment (EGSE) board with Arduino IDE for testing.

Cold gas propulsion module has not been functionality tested as of writing this thesis.

1.3.1 Magnetorquer specific tests

Magnetorquers, or electromagnetic coils (with no core on EC-2), are the fallback actuator for the upcoming mission, meaning that first it needs to be conclusively shown that all operations are possible with the other two actuator sets, before we can steadily start using the magnetorquers again to conserve CGP fuel or desaturate the RWs.

Each magnetorquer needs to be characterised by its voltage-used-to-magnetic-moment-created graph, which is temperature dependent, as the resistance in the circuit and the coil change. Measuring the throughput current gives more hope for a constant relation between the two, but this might also be affected by the sensor measuring the current, meaning it also needs thermal characterisation.

Another thing to test for is the approximate time for the residual current from the coil to diminish below a certain threshold after the voltage has been cut off or changed, which is of course due to Lenz's law. This means that unless the satellite in its final configuration has passed an insane amount of magnetic-field specific calibration testing (meaning functions of magnetometer measurements with both the magnetic field magnitude and temperature but also the currents in all three of the coils as input variables), there is a time period for which in the duration of and a certain time after each coil has been used, we cannot trust any of the readings from most of our magnetometers, which are in close vicinity to the magnetorquers.

These tests can begin as soon as the Engineering Model electromagnetic coil driver electronics arrive. Testing currently planned to start in September (Appendix B).

Chapter 2
Sensor Data Analysis

Overview

Chapter two will focus on working out the calibration methodology and later pipeline for flight model sensor calibration, as in many regards, anything sensor or environment specific cannot adequately be compensated for before the final stack is assembled with the payloads arriving from multiple countries. However, thermal and vacuum calibration and testing can be done beforehand as even with a different sensor unit, the materials, thermal expansion and other electromechanical effects should undergo a similar change and can be extrapolated.

This chapter will present some of the gathered data and the calibration parameters for the tested sensors. Each of the IMU sensors shall receive a template calibration procedure, both for the measurement range and a temperature range. The IMU sensors shall also be tested for vacuum effects in pressures down to 1 Pa. Finally, the preliminary results of the two-axis Sun sensor characterisation will be presented. The actuators will mostly undergo highly specific closed loop testing on the assembled flight model since, with the exception of magnetorquers, the reaction wheels and cold gas propulsion systems are space-qualified hardware, making the task of sufficient characterisation of those systems remain outside the scope of this master's thesis. The different aspects of testing the actuators are covered in both Chapters 1 and 3.

2.1 Data analysis

In this section, the thesis analyses the data gathered in previously described tests. The first sub-section will present a simple and general IMU sensor model, which can be accurately used in

the calibration process of the gyroscopes, magnetometers and the accelerometers. The following paragraphs will give an overview of the respective calibration results, providing us either an equation to calculate understandable real-world values from the somewhat obscure and often completely twisted "sensor units" or at least the correct heading of the unit vector describing the respective physical world quantity such as for example the magnetic field. Calibration of the IMU sensors is followed by an analysis and characterisation of the Sun sensor intensity mapping and FoV determination experiment.

Thermal calibration testing was also completed for all the IMU sensors, giving us the approximate temperature dependency of the calibration parameters. Previous theses done in ESTCube on sensor characterisation or calibration, such as Jaan Viru's "*DESIGN AND TESTING OF ATTITUDE DETERMINATION SENSORS FOR ESTCUBE-1*" [26] or Madis Kaspar Nigol's thesis [16], have followed down the path of calculating the uncertainties from thermal and other effects without a calibration function dependent on temperature (Viru) or fitting a second order polynomial through the sensor readings at different temperatures (Nigol). The author of this thesis finds it best for operational effectiveness and computational simplicity to conclude a full calibration test in different temperatures, giving us the dependency, but foregoing the polynomial fit, as it is a far more complex operation to handle for the satellite's On-Board Computer (OBC) than a linear spline interpolation with no real benefit in measurement accuracy.

2.1.1 Generalised sensor model

This section will briefly explain the reasoning behind following a generalised 3-axis sensor model for standardised calibration purposes.

We first presume that throughout the calibration process we know the **reference value** of the physical quantity: the magnetic field strength, gravitational acceleration or the angular velocity of the testbed. Let this be denoted by c. Note, however, that this sensor generalised sensor model does not define the reference value uniquely, nor does it have to be in SI units. To calibrate the sensors for a normalised unit vector we just have to set our **reference value** to 1. This reference value can later be expanded into a unit system of preference considering the required uncertainties determining said, for example "reference magnetic field value in SI units on this latitude and that longitude." The calibration could still be used without the knowledge of any magnitude, in which case it will simply output a unit vector in the correct direction.

We can arrive at this value if we would know the respective vector components such that:

$$c = \boldsymbol{n^T n}\,, \tag{2}$$

where **n** is the vector of the measured quantity. **n** can be difficult to measure exactly in all three axes, but *c* is usually easy to measure or has a constant value or can as well be set to 1. The 3-axis sensors, however, always measure a vector related to **n**. We can call this vector measured by the sensors axes **m**.

We then evaluate, that each IMU sensor might be affected by a constant offset or a similar defect usually called a **bias** and denoted by the vector **b**, that can shift the sensor's readings linearly in each axis. The sensor might also be affected by differing sensitivities for the axes, the axes themselves may be badly aligned inside the sensor body or there may be cross-axis interference present in the measurements, meaning that activation of one axis produces an offset or 'spill-over' to another. These three effects are referred to as **gain**, and are described in 3D space as a transformation matrix, denoted **G**. The main diagonal of this matrix represents the sensitivity of the sensor while the other elements account for sensor axis non-orthogonality and cross-axis interference effects. Thus, we can write:

$$\boldsymbol{n = G\,(m - b)} \tag{3}$$

as describing the way the sensor measurements can be transformed into the real-world respective vector while the determination of the coefficients for **G** and values for **b** is the calibration. We stipulate that **G** is symmetric, such that:

$$\boldsymbol{G^T = G}\,, \tag{4}$$

and that the values on its main diagonal are positive.

Unable to accurately find the components of **n** during calibration, we next turn back to the real-world quantity *c*, which gives us:

$$c = \boldsymbol{n^T n = (m - b)^T G^T G (m - b)}\,. \tag{5}$$

Before continuing, we redefine:

$$\boldsymbol{K \equiv G^T G}\,, \tag{6}$$

Next we arrive at the calibration function ***J(K,b)***, which is a cost function that aims to minimise the difference between the sensor measurement **m**, and the real-world value *c*, over all instances *i*. The difference is minimised by selecting the right **K** and **b**.

$$J(\boldsymbol{K}, \boldsymbol{b}) = \sum_{i} [c_i - (\boldsymbol{m_i} - \boldsymbol{b})^T \boldsymbol{K} (\boldsymbol{m_i} - \boldsymbol{b})]^2 \tag{7}$$

As the cost function includes the matrix **K**, necessity for the symmetry constraint (6) on the gain matrix **G** becomes clear – we will be able to take the square root of **K** to determine **G**.

Minimising this cost function can be realised in two following ways relevant to our sensors: 1) with a constant known *c* and, 2) a changing, but measurable *c*. The first of these methods is used with the calibration of magnetometers and accelerometers in the presence of constant field strengths. The fixed value of *c* lets us describe this process as a relatively simple ellipsoid fitting operation, aiming to find the best ellipsoid to account for all the data gathered by the sensor on its surface. The three-dimensionality of the problem also tells us of the need to measure the sensor readings in as many orientations as possible, to cover more of the ellipsoid's surface. This idea is illustrated further in Section 2.1.3 – Magnetometer Calibration.

The changing real-world value *c* poses somewhat of a bigger problem, but the same basic principle can be followed with the use of an optimisation algorithm such as any gradient descent or differential evolution based algorithms. The calibration of the gyroscopes using a rotating bench, with a measurable but non-constant velocity due to different mechanical problems, is done just so, using a Python SciPy.Optimize differential evolution library [27]. The results are presented in Section 2.1.2 – Gyroscope Calibration.

2.1.2 Gyroscope calibration

2.1.2.1 Measurement calibration

The calibration of gyroscopes required the data from the rotating bench encoder and the wireless gyroscope to be time synced as accurately as possible for the best calibration results. With regards to the calibration function, the $\mathbf{m_i}$ are the measurements from the EC-2 gyroscopes and the $\mathbf{c_i}$ are the encoder values at the same time. The uncertainty from the 90-cog encoder rotating bench was analysed and is presented in Appendix C.1,

but due to this Chapter focusing on the theoretical template for sensor calibration, it was omitted from further analysis as the sensors calibrated by this bench shall be recalibrated in the future on a far more accurate bench. Therefore, an in depth analysis of uncertainties for a model that demonstrates a high level of fidelity and a low overall error is in author's view not relevant to this chapter. It shall, however, become relevant in the future with the calibration of Flight Model sensors and for the normal functioning of the Unscented Kalman Filter, that handles uncertainties through a covariance matrix.

Following Figure 2.1 presents the results of the calibration function applied to the sensor raw measurements (blue). This is compared in turn to the manufacturer-provided sensitivity calibration values from the datasheet [20] (orange) and the "truth value" from the rotating bench encoder (black).

As can be seen from the figure, the calibrated measurements of the gyroscope follow the constant fluctuations of the rotating bench to a high precision, while the stock option shows errors both above and below the reference value.

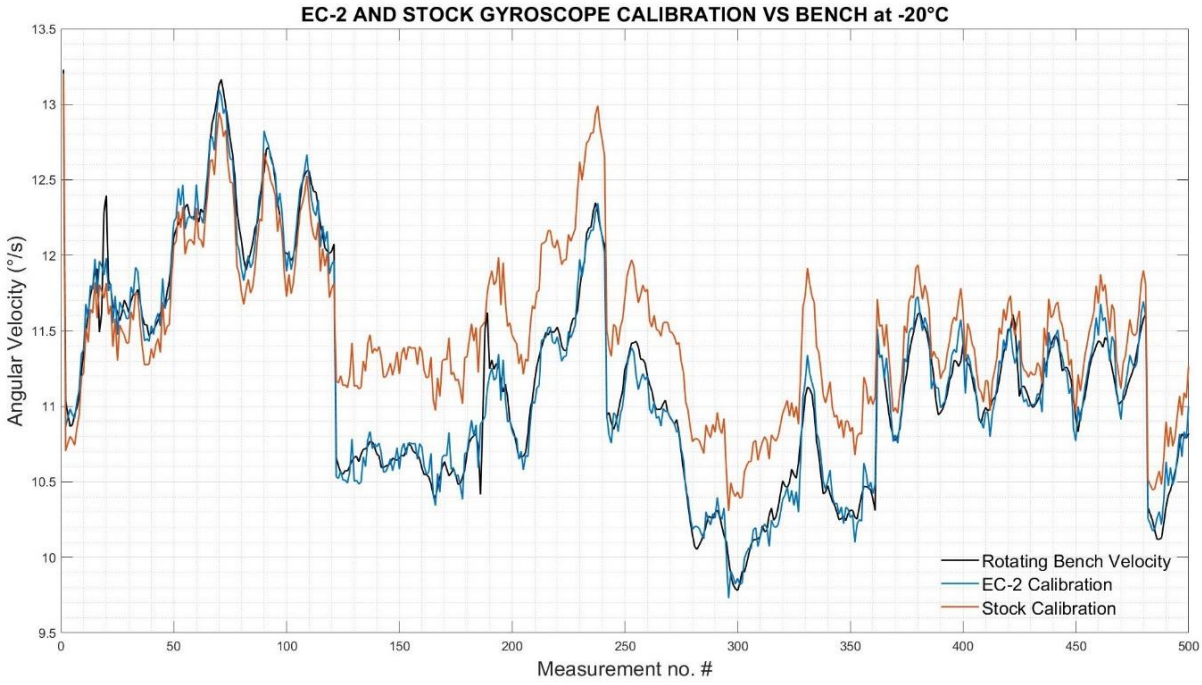

Figure 2.1: Comparison of EC-2 calibration data to stock calibration data and rotating bench encoder data.

The calibrated values for the gains **G** and biases **b** at 20 °C and in the ±125 °/s mode are presented as follows:

$$\boldsymbol{G_{20}} = \mathbf{10^{-6}} \cdot \begin{bmatrix} 3797 & 1.699 & 2.400 \\ 1.699 & 3815 & 1.960 \\ 2.400 & 1.960 & 3820 \end{bmatrix} \quad , \qquad \boldsymbol{b_{20}} = \begin{bmatrix} 4.425 \\ 28.824 \\ 7.878 \end{bmatrix} .$$

Figure 2.2 elaborates on the comparison by depicting the error between the reference velocity of the rotating bench and the one measured by the gyroscopes at different speeds. The necessity for a thorough calibration becomes apparent as the system is exposed to more extreme temperatures, presenting us a visualisation for the need for thermal calibration as well.

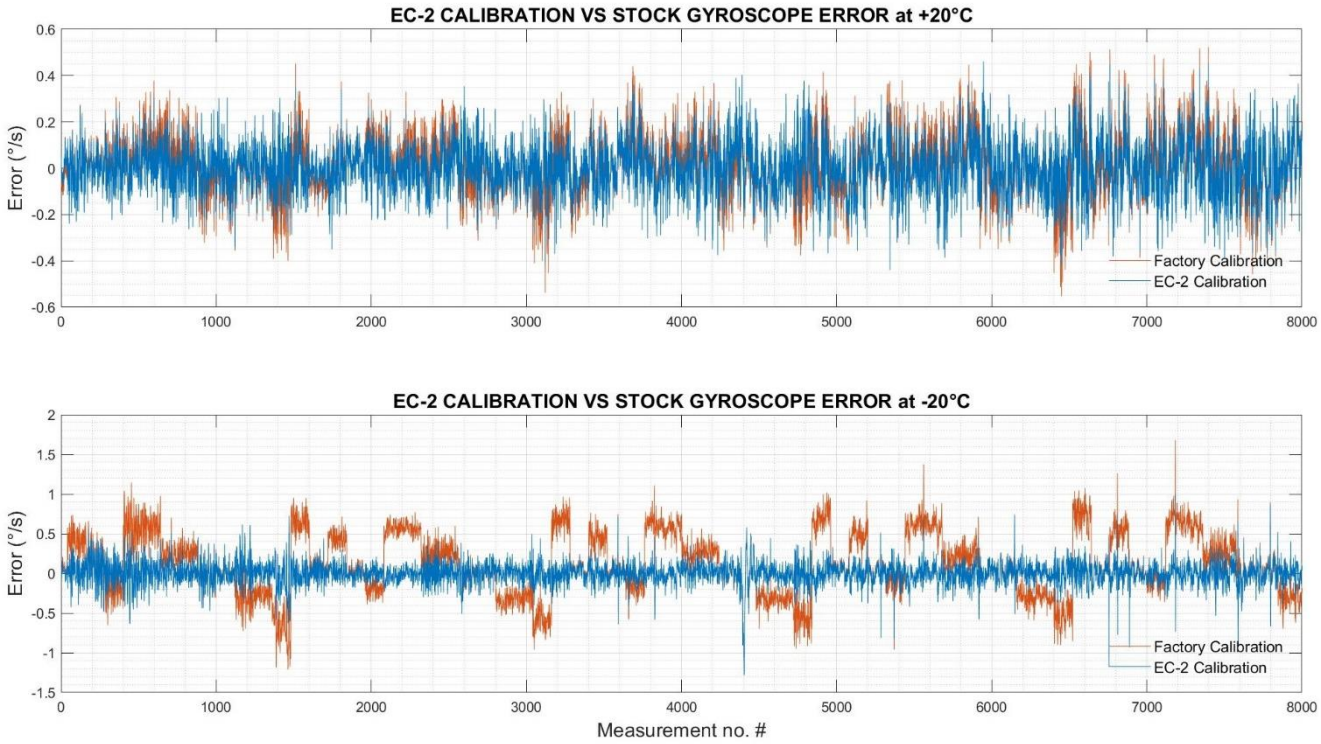

Figure 2.2: Gyroscope measurement errors for EC-2 calibration (blue) compared to factory calibration (orange). Note that the values more or less align at room temperature but vary greatly at thermal extremes.

2.1.2.2 Thermal calibration

The calibration routines were done at four different temperatures, which allows us to visualize the drift in gains and biases due to thermal effects in Figure 2.3. This effect is probably responsible for a large part of the mismatch presented in the bottom graph of

Figure 2.2. The figure does not include the temperature dependency of the non-diagonal elements of the gain matrix, which was also measured and calibrated, but due to its minuscule magnitude is difficult to distinguish form random noise and is not critical. The dependency will be accounted for during the satellite's in-orbit operations.

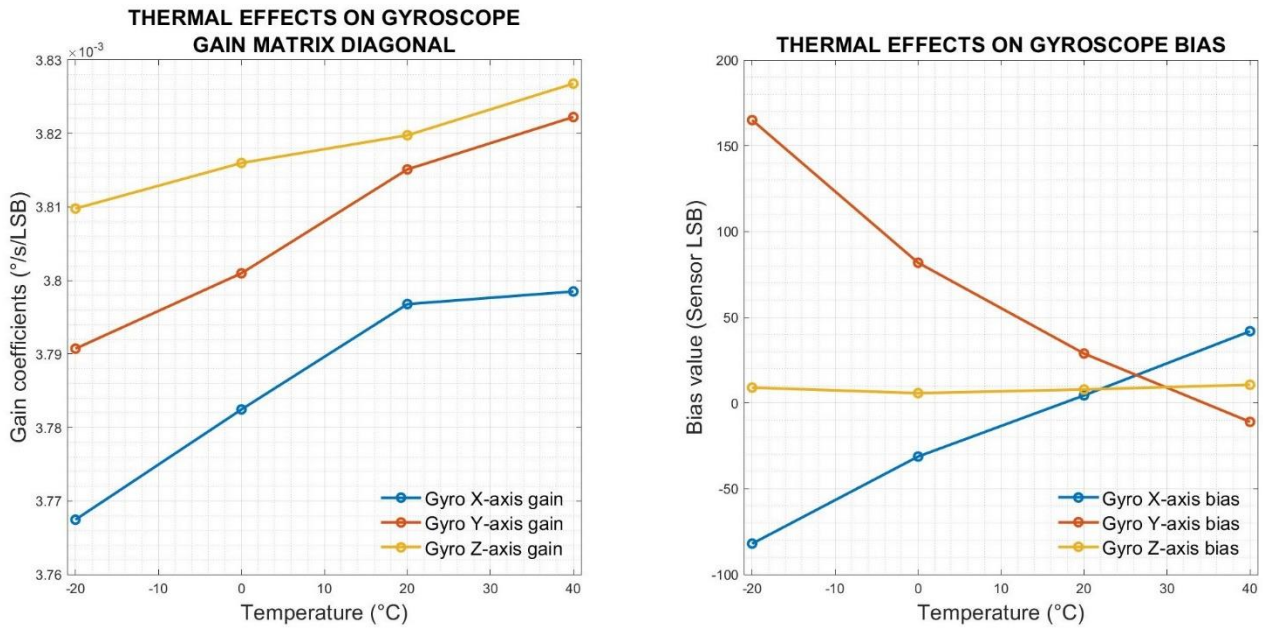

Figure 2.3: Temperature dependency of EC-2 gyroscope calibration parameters.

2.1.2.3 Vacuum effects

Gyroscopes were subjected to room-temperature low vacuum testing (down to 1 Pa) while at standstill. Analysis of the gathered data (Figure 2.4) allows us to estimate if the calibration parameters are also a function of ambient pressure or simply offset by vacuum conditions. This is apparent with the sensors tested for EC-1 [26, Sec.3.7], where only the uncertainty stemming from vacuum was investigated. The data suggests that the vacuum conditions indeed have an effect on the gyroscope readings, though this might be affected by the different resonance modes of the vacuum chamber and its pumps while under vacuum compared to standby. Further testing under higher vacuum (up to 10^{-5} Pa) levels is advised to fully characterise the extent of this dependency.

While the functionality of the IMU sensors were also tested pre- and post-high-vacuum testing, the measurements were not constantly logged. The data is still under analysis.

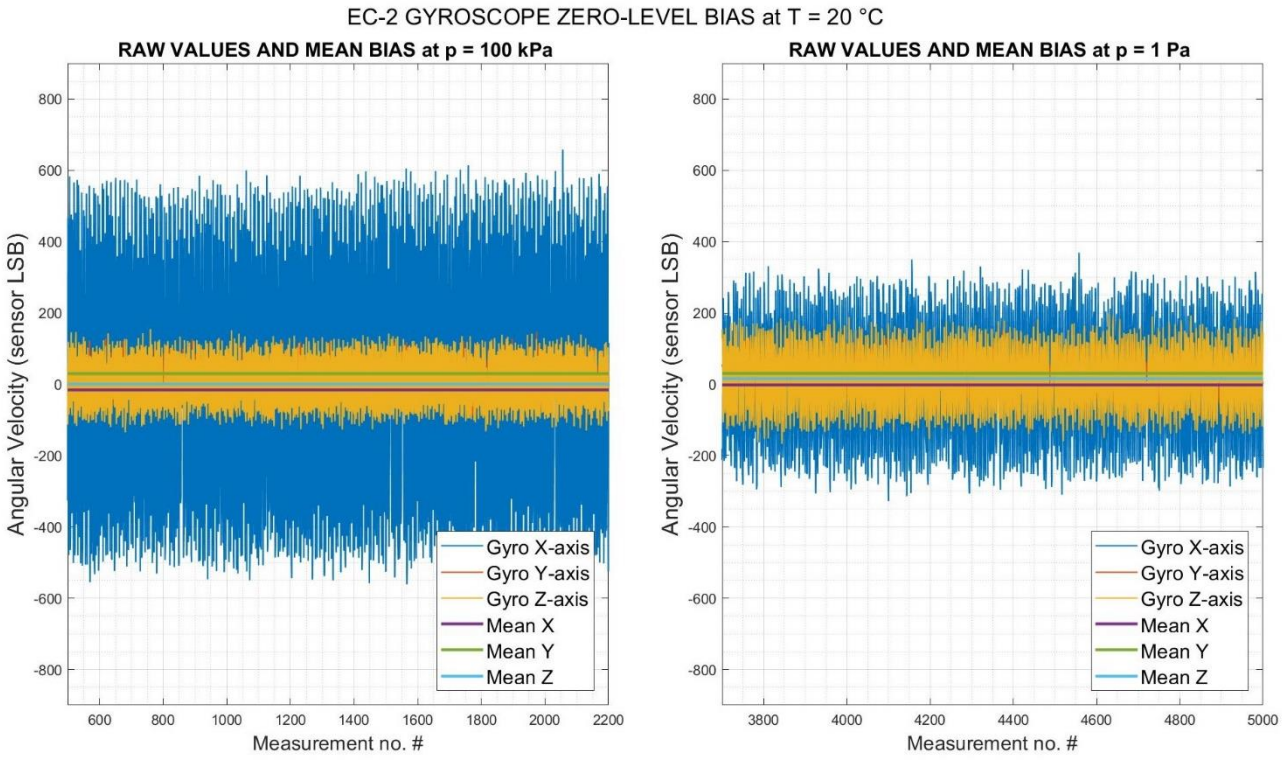

Figure 2.4: Vacuum effects on of EC-2 gyroscope zero-level bias.

2.1.3 Magnetometer calibration

The Magnetic field inside the satellite can only be determined and calibrated for only when the flight model of EC-2 has been fully integrated. While not containing any ferromagnetic materials, the satellite's three reaction wheels and its main electric solar sail payload have internal electric motors that will cause a local magnetic disturbance. The following calibration procedure serves only as a proof of concept and a pipeline for the final calibration.

2.1.3.1 Measurement calibration

Magnetometer calibration follows same generalised sensor model, but unlike gyroscopes, the reference measurement values stay constant throughout the measurement as the magnetic field magnitude or direction do not change for the

duration of the calibration test. This means that gathering calibration data in multiple possible orientations will fill a given volume of 3D-space with a spheroidal point cloud centered on the offset of the sensor. The deviation of the point cloud from a perfect sphere is governed by the gain matrix.

This approach is also well described in more depth in an article by Kok & al., published 2012 [28]. With regards to magnetometer calibration, the gain matrix and bias vectors are often referred to as "Soft-iron" and "Hard-iron" effects, respectively. The following Figure 2.5 is a visualisation of the gathered magnetometer data scattered in 3D-space and its calibrated counterpart. Due to obscure sensor LSB units, the radius of the calibrated sphere and point cloud is stretched evenly for a good visual representation and comparison of the sensor calibration process.

The calibrated values for the magnetometer gains **G** and biases **b** at room temperature and in the '±4 gauss' mode, gathered on a rotating bench are presented as follows:

$$\boldsymbol{G} = \mathbf{10^{-6}} \cdot \begin{bmatrix} 373.6 & 0.106 & 19.42 \\ 0.106 & 369.7 & -4.23 \\ 19.42 & -4.23 & 340.8 \end{bmatrix} \quad , \qquad \boldsymbol{b} = \mathbf{10^{3}} \cdot \begin{bmatrix} 3.349 \\ -9.402 \\ 2.646 \end{bmatrix} .$$

Following Figure 2.6 shows the same dataset in comparison to the stock calibration with the bias subtracted by us for a more justified comparison. As can be seen from the red/grey ellipsoid on Figure 2.5 and also from the gain matrix above, a single-value "sensor LSB to measurement" calibration could never be able to account for the tilt and elongatedness of the ellipsoid.

2.1.3.2 Thermal calibration

Thermal calibration of the magnetometer coefficients and bias, presented on Figure 2.7, followed the same basic procedure as the thermal calibration of gyroscopes but due to the strong magnetic disturbance of the iron rotating bench, the data was gathered at standstill, without the bench. It is important to note, that the gathered data still cannot be strictly analysed and taken at face value as one has to also account for the magnetic field caused by the thermal chamber's iron structure and various motors and pumps even though the chamber was shut down for the duration of the calibration and care was taken to place the sensors as centre as possible in the chamber. Only the relative change is to be noted from this calibration step.

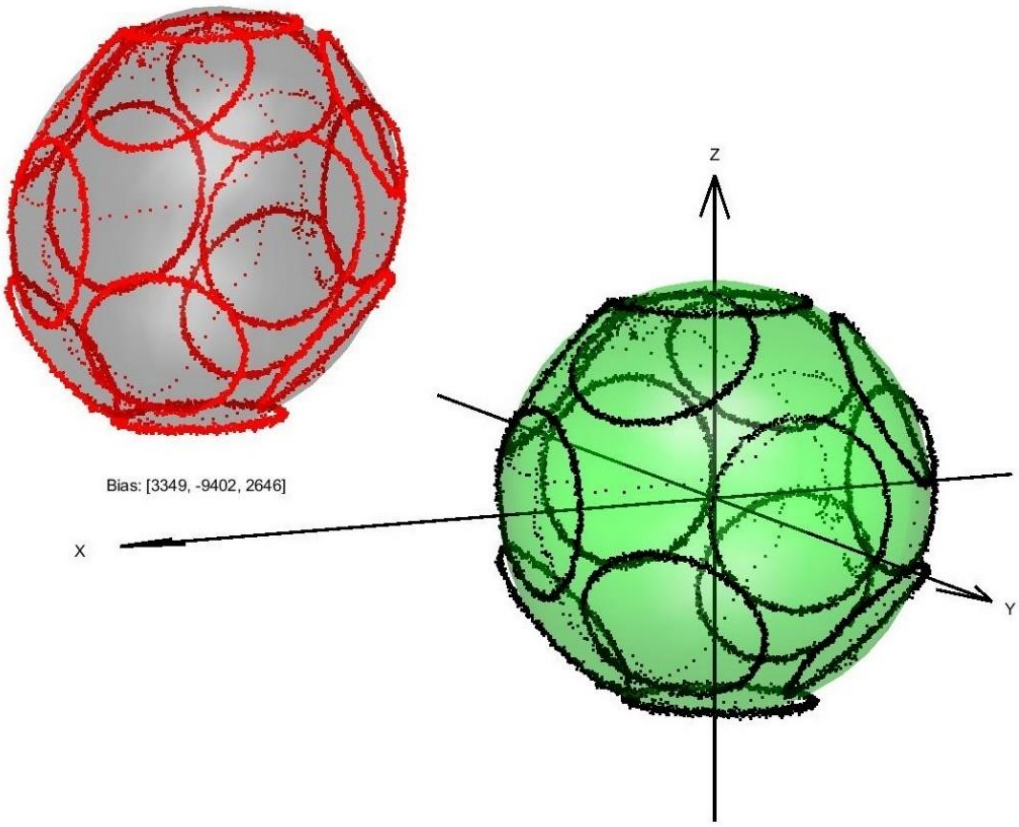

Figure 2.5: Uncalibrated raw magnetometer values (red) with a fitted ellipsoid (grey) compared to the calibrated data (black) and their respective 'sphere' (green). Note that the calibrated values have been magnified to be comparable to raw sensor data values.

Considering the small shift in sensor position when shuffling through the necessary orientations or tiny shifts of the sensor position between temperature changes, it is hard to distinguish general, if any temperature change in the hard-iron bias of the magnetometer. The soft-iron effects of the gain matrix show more thermal volatility, although $\mathbf{G}_{yy20}$ seems too sharply out of place to be considered part of the temperature curve. As flight model magnetometers need to be recalibrated before flight and most probably even post flight, any problems with the Engineering Model data, will not concern the mission.

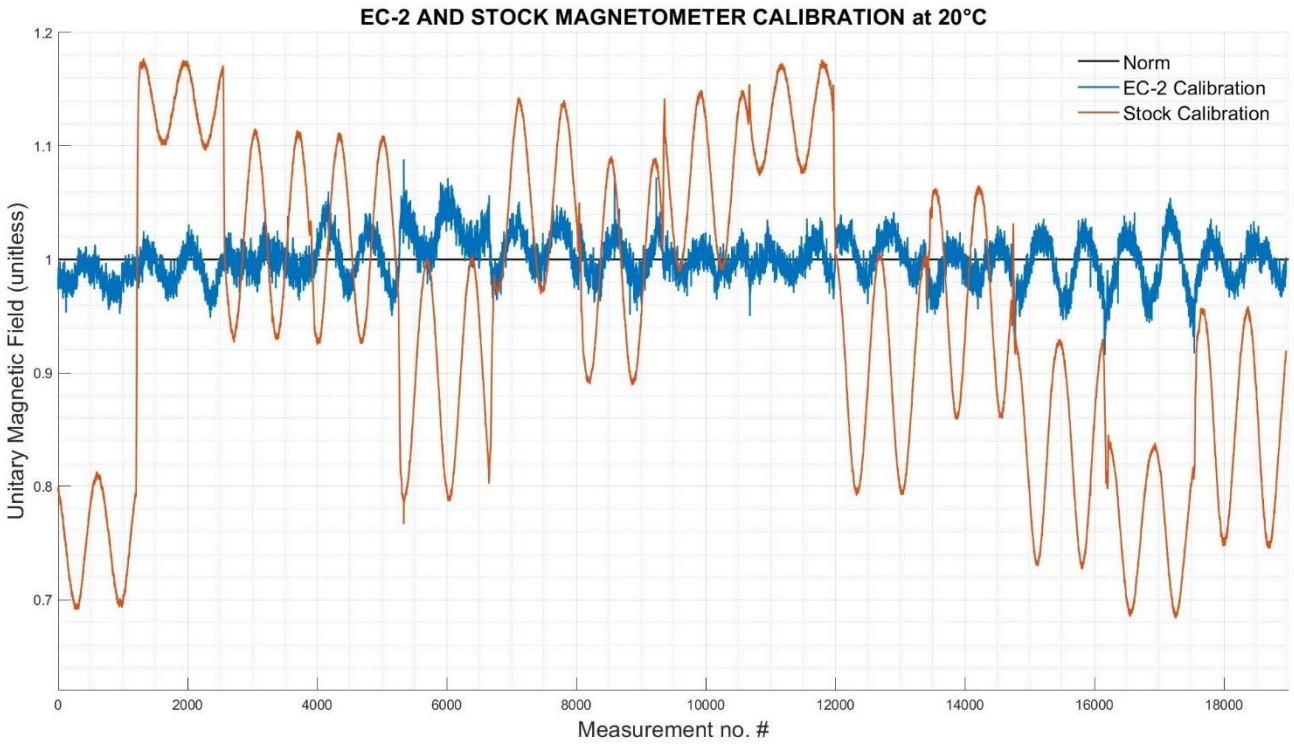

Figure 2.6: Magnetometer calibration comparison of EC-2 to stock calibration with the bias subtracted for a fair comparison. The data is also 'normalised' to a total magnetic field strength of 1 u.

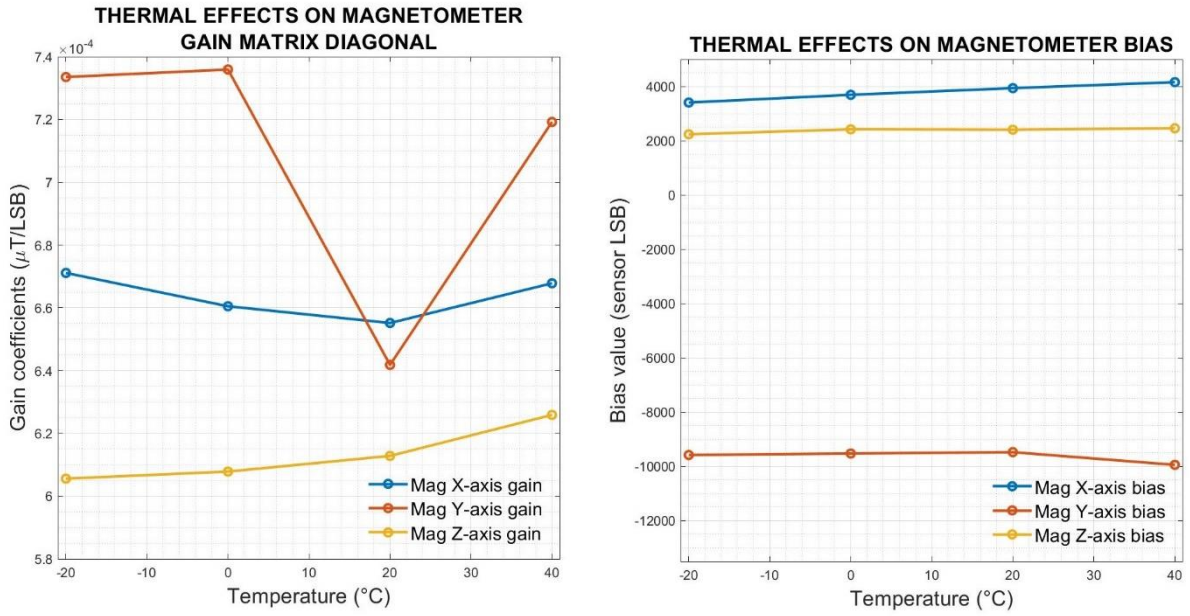

Figure 2.7: Magnetometer EC-2 thermal calibration.

2.1.3.3 Vacuum effects

Vacuum calibration of the magnetometers was also unsuccessful, as the gathered data on Figure 2.8 shows a sharp jump from the normal 4100 LSB unit level up to 4800 LSB as the vacuum pump is activated, around measurement no. 3000. This change is too instantaneous to be anything other than the offset from a new external magnetic disturbance, this time by the starting of the electric vacuum pump motor apparently in close proximity. This shift was also apparent and similar on other axes. Further vacuum calibration testing is required, and it should take place as part of the thermal vacuum testing with the flight model assembled. The larger thermal vacuum chamber also hosts its vacuum pumps a bit further away from the metal test chamber, which helps with getting a reference reading from the magnetometers in vacuum conditions.

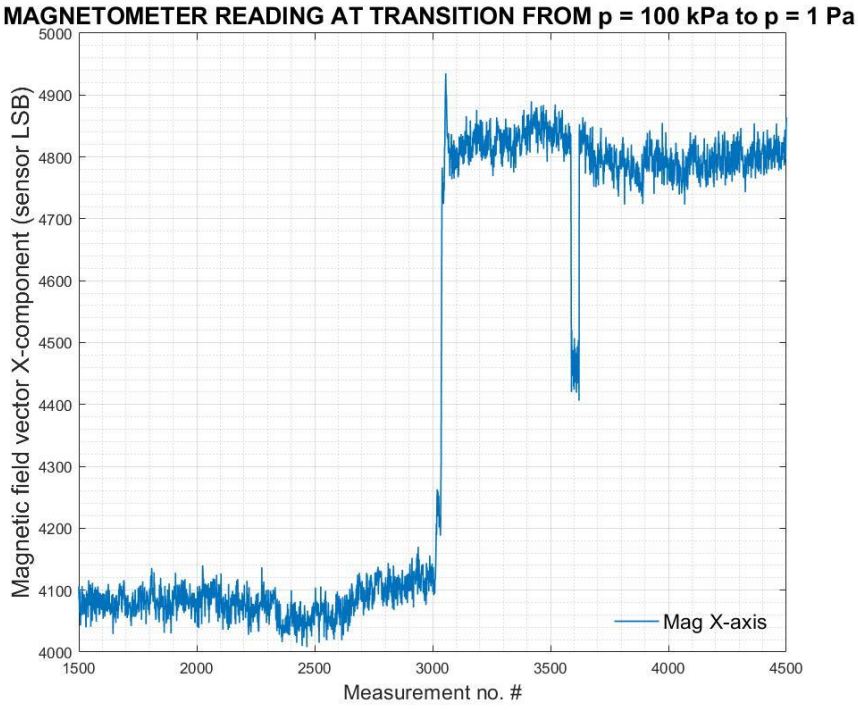

Figure 2.8: Magnetometer raw data readings at the moment the vacuum pump was turned on.

2.1.4 Accelerometer calibration

Accelerometer calibration follows the same basic pipeline as magnetometer calibration, with the critical difference that the known gravitational acceleration reference value can be used if the sensor is kept completely still during calibration.

2.1.4.1 Measurement calibration

Apart of the magnetometers, the accelerometers show little to no major offset (or bias) in their readings, meaning factory calibration would do a good enough job of pointing down terrestrial uses. Space applications, however, envision us using it in a micro-gravity environment and to sense minuscule Cold Gas Propulsion (CGP) thrusts or antenna and extendable solar panel array deployment on the sides of the spacecraft.

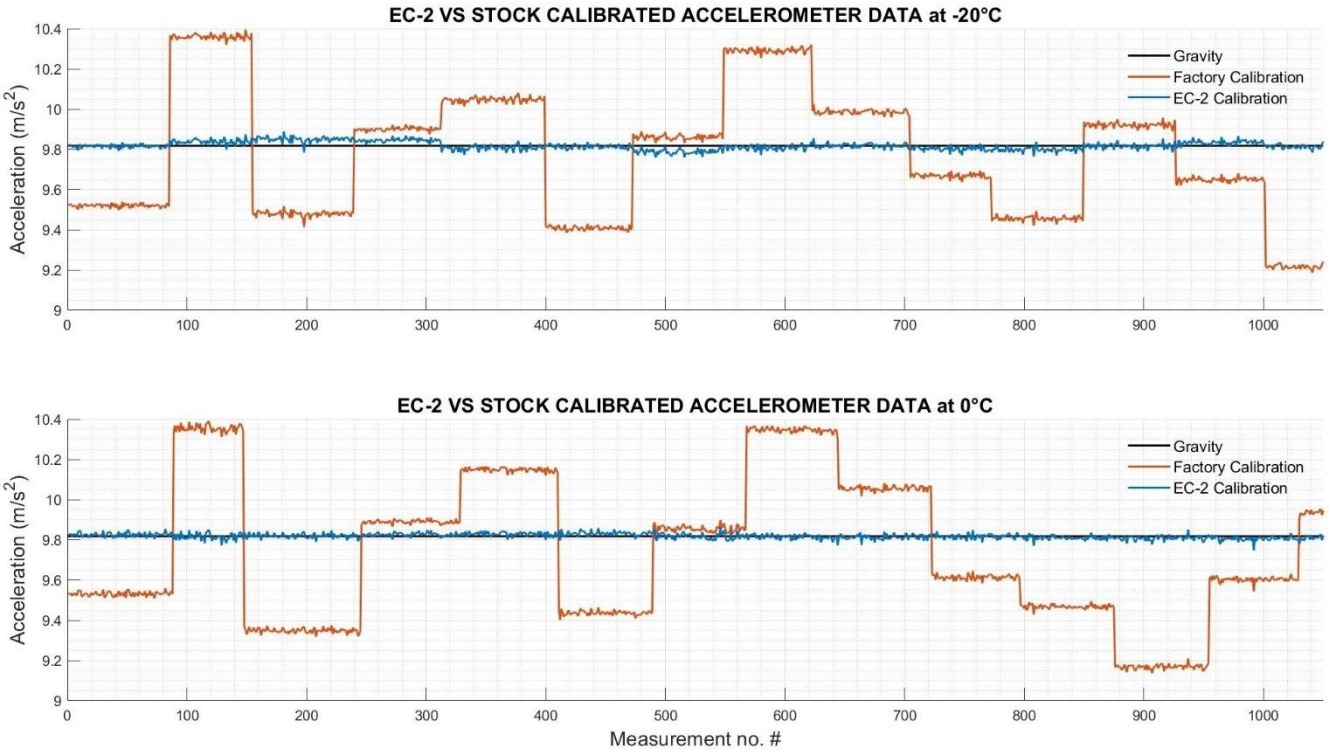

Figure 2.9: Accelerometer calibration comparison of EC-2 to stock calibration. Note that the gravitational acceleration used for Tartu in the figure is 9.81766 m/s^2, but this is simply a trivial scaling factor for both data up from '1 g'.

The immense magnitude of the gravitational acceleration in comparison to our measurable accelerations makes the complete calibration of the accelerometers on Earth a difficult task, usually requiring highly specific and long drop tests, while orientation is changed to introduce centripetal acceleration to the sensor system to be calibrated against. This implies the need to recalibrate the accelerometers in true orbital micro-gravity before any trust can be placed in their readings under truly extreme conditions. This is discussed further in Chapter 3. However, in order to try to characterise the sensors before in-orbit calibration, we present our calibration for the accelerometer under normal gravity in Figure 2.9. The calibrated values for the accelerometer gains **G** and biases **b** at room temperature and in the ±2 g mode, gathered at standstill are presented as follows:

$$\boldsymbol{G} = \mathbf{10^{-6}} \cdot \begin{bmatrix} 2440 & -1.876 & -1.336 \\ -1.876 & 2368 & 4.939 \\ -1.336 & 4.939 & 2420 \end{bmatrix} \quad , \qquad \boldsymbol{b} = \begin{bmatrix} 97.65 \\ -156.6 \\ 194.7 \end{bmatrix} .$$

Note the relatively small bias, the similar values on the main diagonal and the equally minuscule values off the main diagonal of the gain matrix.

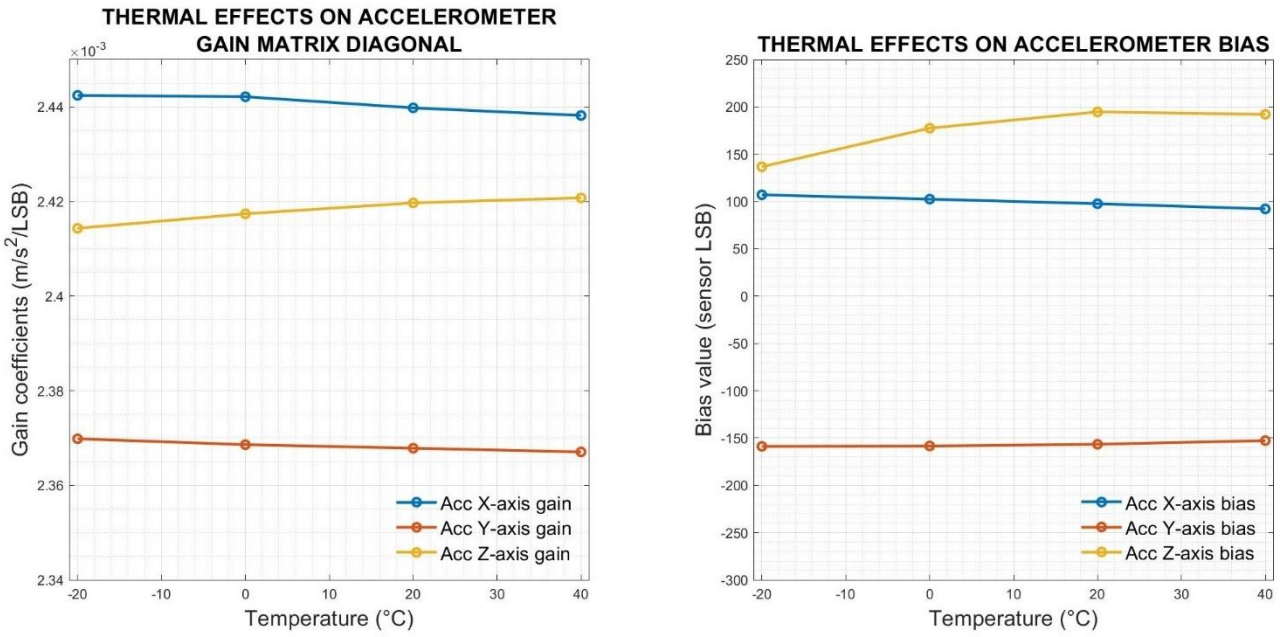

Figure 2.10: Accelerometer EC-2 thermal calibration.

2.1.4.2 Thermal calibration

For the most part, thermal calibration of the accelerometers presented on Figure 2.10 shows good linearity and no major thermal effects aside the change in bias for accelerometer Z-axis.

2.1.4.3 Vacuum effects

As sufficient precautions conducting the test were not followed and data was not logged in steps at different pressure levels with the machine turned off, the shift seen in the data on Figure 2.11 is therefore undistinguishable between vacuum effects on the sensor and changes in readings due to vibrational modes. A new test procedure needs to be considered with the sensors detached from the vibrations of the vacuum chamber. This might be viable for the large thermal vacuum chamber, but that in turn complicates data logging. The use of accelerometers in not mission-critical for EC-2 and while further testing is needed, it is unlikely that specific testing of the accelerometers will be done apart from the full thermal vacuum tests of the flight model towards the end of the year.

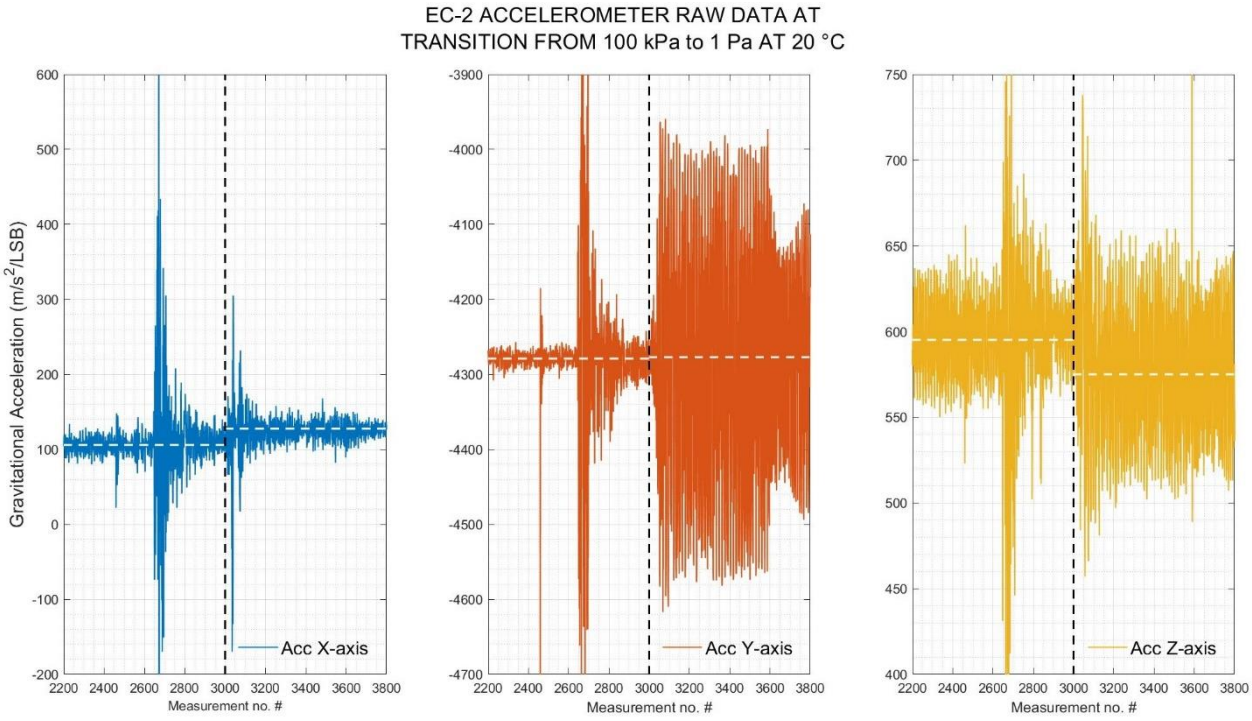

Figure 2.11: Accelerometer raw data readings transitioning into a low vacuum environment. White dashed lines represent the averages before (# 0 to 2600) and after (# 3400 to 5000) vacuum pump initiation, while the black dashed line (meas.# 3000) shows the approximate time of vacuum pump initiation.

2.1.5 Sun sensor characterisation

2.1.5.1 Two axis intensity mapping

This test allows us to characterise the new design of Sun sensors in its full form as they will be used on the satellite. Figure 2.12 shows the sensor intensity response over the whole range of the two perpendicular single-axis Sun sensors combined. This is achieved by automatically selecting for images that clearly have both peaks visible and above the dark current noise threshold (~660 sensor units), meaning in essence selection for intensities greater than 700 u. Euclidean norm was found from those two intensities, finally giving us the x, y and z coordinates for the plot.

Pinpointing the sensor pixels with max intensity response gives us the pixels [569, 605] for the peak location whereas the location [512, 512] would be the expected value. This could be called the “centre” of the sensor field of view, as presumably this is where the light source is at zenith relative to the sensor. The deviation, however, can be explained by many things starting from the misalignment of the sensor frame at the beginning of the test, any of the connections fixing the sensor board to the rotary stages, misalignment of the mask covering the sensor or even the soldering misalignment of the CMOS sensor itself inside the Sun sensor. The following Figure 2.13 depicts the same data as a 3D surface plot.

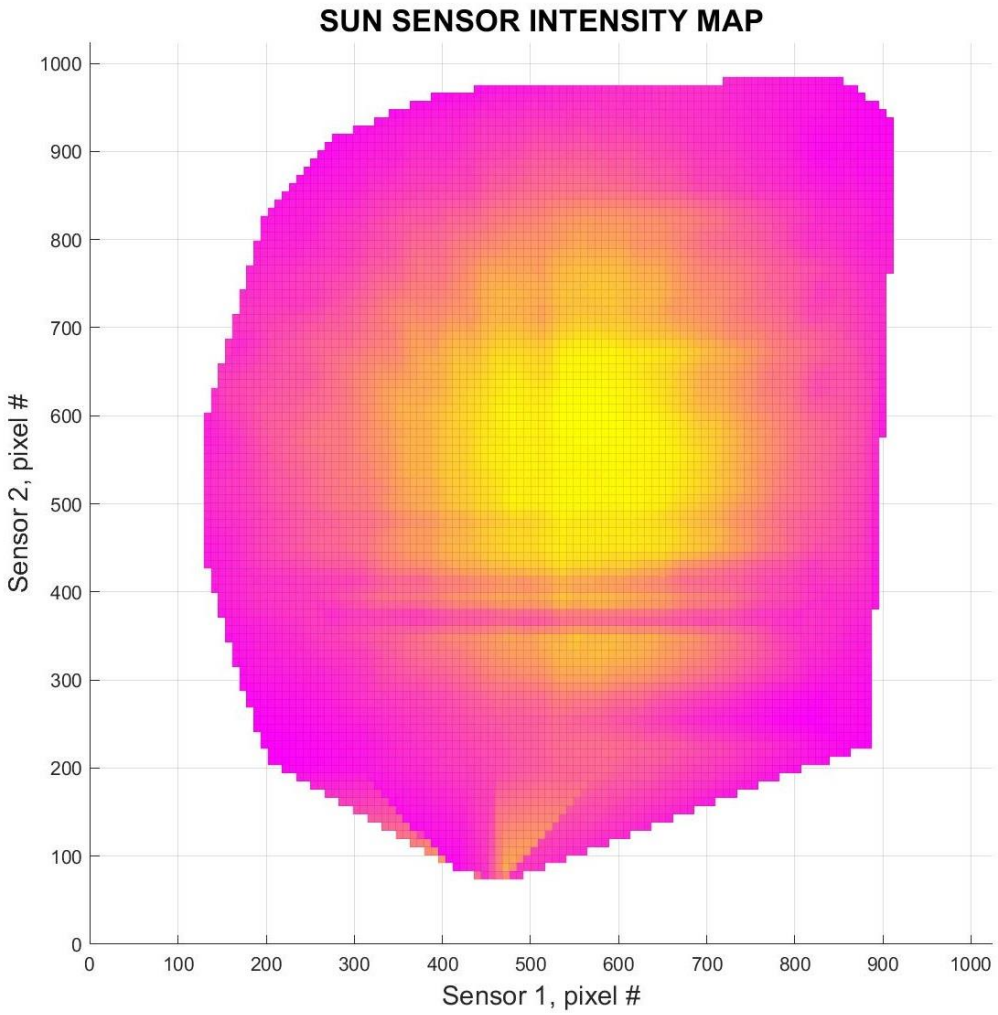

Figure 2.12: Sun sensor intensity map for correlated data from both of the sensors. The presented figure shows a mechanical disturbance in the sensor resulting in temporary dimming of the light source at two certain angles. Also visible is an internal overflow near bottom of the plot.

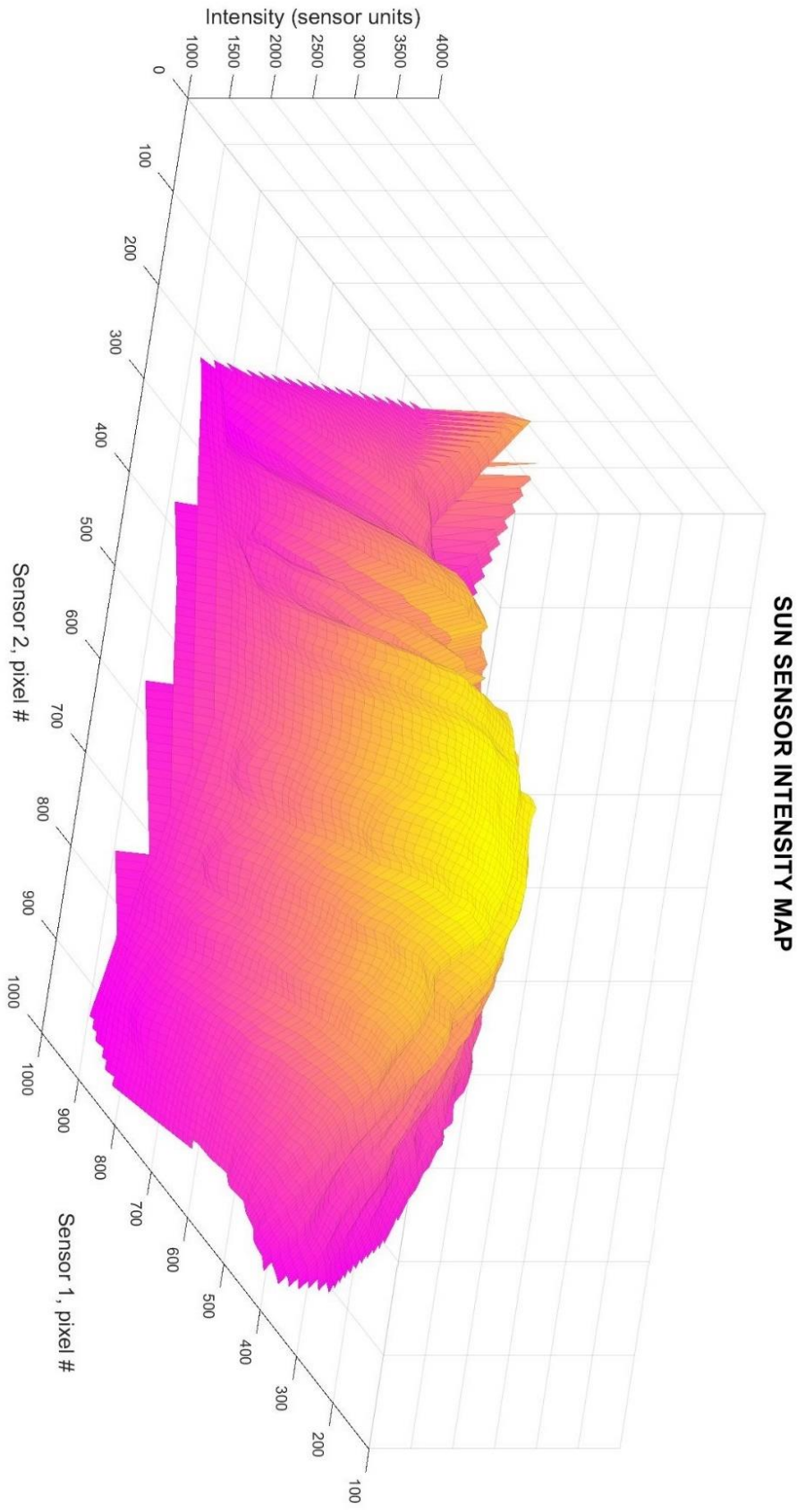

Figure 2.13: Sun sensor intensity map from (Fig 2.12) as a 3D surface plot.

More things to note in Figure 2.12 are the two sharp fall-offs of intensity around pixels # 400 of sensor 2. These might also be due to various different effects, some of which include 1) random non-uniformity of the precipitated titanium layer coating the sensor, 2) mechanical blockage of the light by sensor mask structure, 3) internal problems with the sensors, dead pixels, etc, however, unlikely; 4) problems with the test setup, which were also encountered, for example, where one of the sensors was blocked off from the light source at certain larger angles (most likely visible at [500, 100]). This does not however explain the intensity regrowth further from zenith at larger angles of incidence.

Another problem lies with the strong intensity response registered well outside the sensors predicted visibility range near the lower portion of Figure 2.12. The origin of this measured intensity is for the moment completely unclear and would need a specific test designed just to understand if what we're seeing is 1) a case of bad internal reflections, 2) a case of bad external reflections, 3) spill-over from the cavity under the mask of the other Sun sensor, 4) faulty data logging and/or shifted pixels.

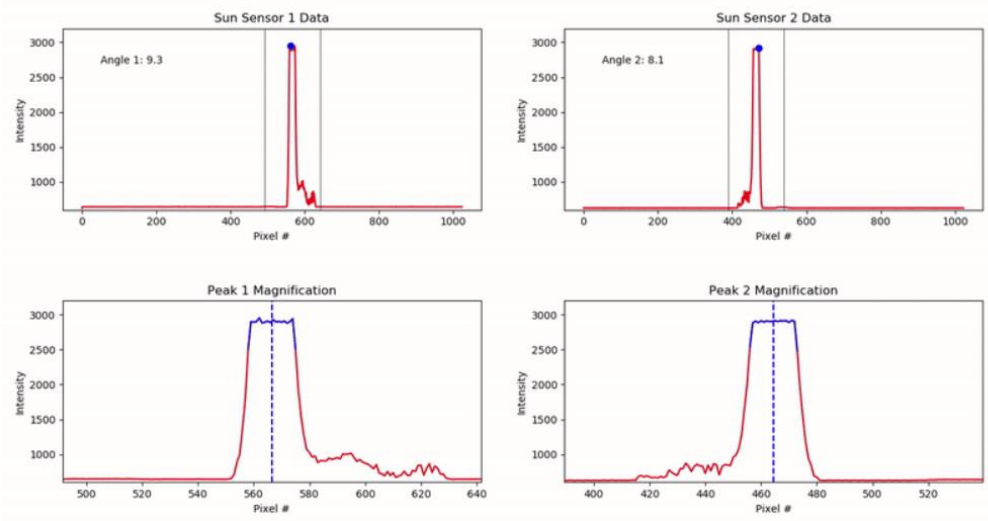

Figure 2.14: Screen capture from the Python code logging data from the Sun sensors in real time. Vertical axis shows the measured intensity in sensor units. This exemplifies the meaning of accounting for all pixels (blue solid line, bottom plots) with intensities at least 70% of the max value (blue dot, top plots), allowing us to calculate the peak location on half-pixel accuracy (blue dashed line).

Further analysis allows us to find the peak centre on a half-pixel accuracy simply by finding the average of all the pixel values that have an intensity reading of at least 70% of the max pixel intensity value. This successfully filters out everything but the peak itself and the mean is easily calculatable. A clarification of this is presented on Figure 2.14. After finding the peak locations on a half-pixel accuracy, we can use this to compare the calculated value of incident light from the Sun sensor with the reference value of incident light known from the optical bench and rotary stage setups. This information could be depicted similarly as a surface plot showing the errors between the two angles. This analysis is still ongoing during the writing of this subsection.

2.1.5.2 Predicted Field of View

Figure 2.15 shows the intensities for both sensors along and across their main CMOS sensor pixel axis, which is just aligning the sensor perpendicular to the light source and then tilting one of the axes, keeping the other centred, and then repeating the process the other way. This data, however, was extracted and pieced together from the large scale two-axis testing routine. The predicted FoV for the sensor on its main axis seems to roughly be ±55° reliably while at least ±45° across axis. Note the lower intensities of sensor 2, which might be caused by 1) a thicker titanium coating on the Sun sensor or 2) the fact that the Sun sensor 1 was picked to be aligned with the light source.

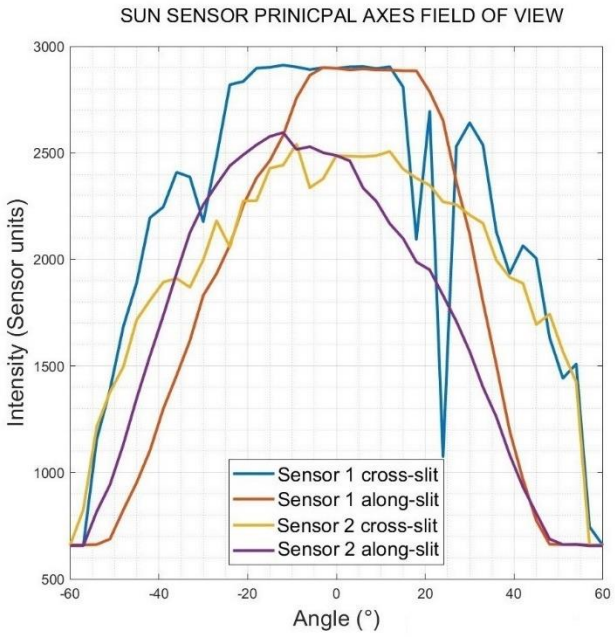

Figure 2.15: Sun sensor field of view along the principal axes of the sensor.

Chapter 3

AOCS Evaluation and Flight Model Testing Campaign

Overview

An important goal this thesis is to recompile and renew the set of requirements relevant to AOCS components and algorithms. Having a traceable requirement-and-verification process is critical for any mission to be successful, as can be seen from the heavy emphasis on bureaucracy and documentation set in place by ECSS and therefore ESA, which has permitted them to conduct incredibly successful space missions for decades.

The first section of the final chapter of the thesis will reiterate the need for EC-2 to pursue a more thorough documentation setup, which would help eliminating any last-minute integration errors or mismatches and tie the project closer together into one well-working unit, as people in different subsystems would finally start to grasp their place in the bigger picture and close links to every other subsystem on the satellite. The second part of this chapter will briefly discuss ESTCube-2 Flight Model qualification testing and calibration, much of which is based upon the AOCS testing plan presented in Appendix B. This in turn relies on Appendix A, which is composed of requirements in the following paragraphs.

3.1 AOCS requirements and evaluation

Compilation of requirements for the subsystem was last sufficiently covered by Hendrik Ehrpais in his master's thesis [22] with quite an untraceable mind map, dating 3 years ago. Of

this, we can reformulate and give a correct designation to a number of requirements that have already been achieved, also requirements what are being worked on or are still relevant and omit some requirements that we have moved away form, that are redundant or have been superseded by other requirements. More recently an internal ESTCube-2 overview document was compiled, listing satellite and payload-specific general requirements. Using these two documents as a basis, one of the outputs of this thesis is a list of confirmed and sorted AOCS requirements in Appendix A, which will also be the basis of the testing campaign.

The first short part of this section lists and gives a justification to any omissions or combining of requirements in AOCS, before talking through the evaluation of the subsystem overall and listing strategies, dependencies and key notes to consider when working towards or testing for each set requirement during Flight Model testing campaign.

3.1.1 AOCS requirements

The following nomenclature is used in the following paragraph: (HE) for the thesis of Hendrik Ehrpais and (ID) for EC-2 Internal Documentation on mission overview. **Bold** is used for kept requirements. *Italic* is used for omitted requirements. ***Bold Italic*** is used for reworded requirements.

Lifetime – *The satellite is expected to have a lifetime of up to 2+ years* (HE). This is an extremely difficult requirement to pitch, as to the authors knowledge there has not been any durability or stress testing of the electronics lasting months or even weeks. This will be omitted from AOCS requirements due to being impossible to test for.

Power – As this has not been completely clarified top-down, it will be briefly discussed. **Peak power usage of EC-2 AOCS sensors shall not exceed 0.5 W**. This is considering 12 Sun sensors at 0.03 W typical power use each with the IMU sensors using next to nothing. Total peak power usage of AOCS actuators could become an issue without sufficient power management. **Peak power use of 3 magnetorquers shall not exceed 12 W à 4 W** (ID). This is the only verified power limitation set on the AOCS actuators. RWs typically consume under a watt and CGP under 2 watts.

Redundancy – **All sensors shall be redundant**, and **failure of one actuator and sensor shall not prevent the main objective** (HE). Redundancy is built into two

separate sets of IMU sensors, with two gyroscopes each. There are extra magnetometers on side panels. The triple actuator systems are also redundant.

Thermal – **Operational range for AOCS shall be -20 to +40 °C. AOCS shall withstand -40 to +60 °C range.**

Mechanical – **AOCS shall withstand Vega-C launch profile.** (ID) *Withstand 17 g random vibration and 16 g low frequency vibration.* (HE) Superseded by determining a launch vehicle. **AOCS shall withstand LEO vacuum conditions.** (ID)

Data processing and logging. – *Diffraction analysis* (HE) is omitted due to Sun sensor design choices making it impossible to detect diffraction. ***Sensor data shall be possible to be logged for analysis on the ground.*** (HE) Logging only 5-10 pixels on each side of the Sun sensor peak will not help a saturated peak or other problems. All data must be logable. **AOCS algorithms run on STM32F7.** These must have a prerequisite in OBCS.

Sensors – **All sensors shall use SPI. All sensors shall use 3.3 V.** ***Sensors shall be housed on OBCS and SP.*** (HE) Sun sensors and magnetometers housed on side panels. ***All sensors shall have preliminary calibration before launch.*** (HE) Some things cannot be calibrated on Earth. **All sensors shall have temperature calibration. All sensors shall measure faster than 10 Hz.**

Sun sensors – *Initial image processing must be done on MSP430* (HE). MCU changed to STM32L4. ***Sun sensors shall have a dedicated MCU for initial image processing.*** **Height of the SS shall be under 4 mm.** ***Sun sensor slit width shall be <= 100 µm.*** Fixed at 100. **Screws shall be glued. Sun sensors shall have a FoV of at least ±45°.**

Actuators – ***MTQ size shall be under 250 x 67 mm and 83 x 80 mm***. (HE) Discussed with STR team who found us more space. ***MTQ shall use 10 V from regulator.*** No raw battery power anymore. ***CGP size shall be 0.3 U.*** (HE) No extended tank. **RW size shall be 25x25x15 mm. RWs shall use 3.3 V. MTQ shall provide at least 0.5 Am^2 of moment. Actuators shall provide enough angular momentum to deploy 11 m of tether.**

Control – **AOCS shall be able to point the satellite with a 0.25 deg accuracy.** (ID) **Pointing stability shall be under 0.125 deg/s.** (ID) **AOCS shall be able to detumble. AOCS shall be able to spin up to 360 deg/s while preserving pointing accuracy of**

up to 3 deg. (ID) *Detumbling should decrease spin rate to operator specified value.* Superseded. ***AOCS shall be able to perform in 5 different configurations: 1) MTQ, 2) RW, 3) MTQ+RW, 4) MTW+RW+CGP, 5) RW+CGP***. (HE) First is the safety-net, third is the normal mode. Second should be used for any camera pointing or calibration manoeuvres and then desaturated on third. Fourth might end up being used for E-sail experiment. Fifth is to be demonstrated for missions outside magnetosphere.

These requirements and a handful of others have been composed into EC-2 AOCS REQUIREMENTS and are presented in Appendix A. The large number of unavailable source requirements is due to some of them serving as AOCS internal requirements, but a good number come down to poor documentation and communication between the satellite's subsystems. While this might be let slide working together on a day-to-day basis as a small group of people, it is bound to cause issues in the long term for EC-2 and would very quickly doom a larger project with several small development teams that do not have constant contact with the other teams. It is therefore critical to start the revision of requirements for other subsystems before the Engineering Model is complete and can be tested.

3.1.2 System evaluation

Looking at the satellite for a moment with a narrow mind, the author considers the AOCS subsystem as a whole and especially its hardware to be taking shape in good time. With the sensors actively passing preliminary thermal and vacuum qualification testing as well as demonstrably improving in measurement accuracy with its temperature calibrated IMU sensors compared to uncalibrated ones, the burden of proof is set next on the attitude determination algorithms to tie everything in the subsystem together on AOCS side, and show that the mission requirements are achievable. The author has functionality tested the RW-s personally, wound the electromagnetic coils of the magnetorquers and has been present at the development and testing of the coil driver hardware, which leaves little to no doubt about the capability of ESTCube-2 in its actuator department. It is soon once again up to the AOCS software to start the closed-loop system testing, with the sensors and Unscented Kalman Filter (UKF) analysing attitude data and the actuators correcting for it through simple control algorithms in preparation for fully fledged Flight Model attitude control testing. Mission success probability is increased

further by full redundancy in the AOCS subsystem, where losing no one senor and actuator will hinder the mission to any great extent.

From the sensor calibration point of view, the basic principles for the calibration of each IMU sensor have been set, which can be followed for the calibration of all the subsequent sensors up to the Flight Model. The analysis of Sun sensor is ongoing, and some mathematical issues need to be solved for before the real errors can be graphed. The thermal characterisation of the Sun sensors is scheduled in late August, which will conclude the preliminary AOCS sensor testing campaign. There is however a problem with evaluating the sensor attitude determination and pointing capability without the UKF machinery behind it. It is clear that sensors themselves cannot be solely relied upon to deliver the set requirements for example for camera pointing and stability, for which one would use statistical methods like the UKF to refine the measurement with the previous prediction and in turn predict the next timestep. This, however, has not yet been simulated or tested for as the focus of the whole of ESTCube-2 is on completing the necessary hardware for flight qualification.

Next to consider are the actuator capabilities to deliver everything that the mission requirements have set. This can only be verified on a theoretical level, given that the actuator kit available to us is completely functional. The preliminary functionality of the most critical actuator systems have been verified, with still work to do on the Cold Gas Propulsion. On a theoretical level, the actuator capability was amply demonstrated by the simulations done by the author and Robert Märk for the article on ESTCube-2 science mission overview mentioned in Chapter 1.3 [5]. The simulations focused on achieving the requirements for E-Sail deployment using only RWs and the CGP module without magnetorquers, while fuel consumption and pointing stability were also under thorough consideration. Relying on the work done on functionality testing and theoretical models, but also the relative simplicity of control algorithms compared to determination algorithms gives the author full confidence in EC-2 actuators for a fully successful science mission.

Everything discussed above should still be taken in its true context, which is as a part of the whole satellite – AOCS is not alone responsible for the success of this mission. The AOCS algorithms rely on the OBC for calculations and the three AOCS actuators are perhaps responsible for the majority of the entire satellites power budget, meaning they rely the most on the Electrical Power Subsystem. The AOCS is not planned to have any autonomous capabilities, meaning that each orbital operation workstack needs to be uplinked to the satellite

through the use of the communications subsystem. A fault in any of the ‘trifecta’ of satellite subsystems would also prove a catastrophic failure for AOCS even if other two remain completely functional.

3.2 Flight Model AOCS Testing

As discussed in previous chapters, there are things that can and cannot be sufficiently tested and calibrated on Earth as the conditions needed might be nearly unattainable. Therefore the following section is divided into two subsections, with the first one establishing tests that need to be completed before launch and the second elaborates on sensors and actuators the calibration of which can be improved once free of the conditions on Earth. One has to keep in mind that ESTCube-2 is a relatively tiny, opportunity- and crowd-funded project of volunteers and as such will aim to cut major corners with any large budgetary expenditures, which a drawn-out testing phase no doubt is. As the development and testing phases compared to big space missions are so compressed, it means that following the complete ECSS guidelines for example for spacecraft testing, propulsion or AOCS [4] with a small team is, in essence, impossible. This fact is understood by ESA very well and thus a separate set of documentation has been produced to account for ‘the high level of integration’ and ‘reduced complexity’ of CubeSat missions. The “Tailored ECSS Engineering Standards for In-Orbit Demonstration CubeSat Projects” [9], latest revision issued in 2016, should be considered the benchmark to strive for in any IOD CubeSat project and that shall be the case with EC-2.

3.2.1 Pre-launch Flight Model testing campaign

Considering the whole mission, the biggest bottlenecks of AOCS success might come from the ability to withstand launch profile vibrations and also the thermal fluctuation extremes between the eclipse and after an hour in constant full sunlight. These two major factors can be extensively tested for by means of vibration testing of the whole satellite Flight Model and by running complete thermal vacuum cycle tests on same Model. Core functionality must remain even after the most inopportune launch profile and longer-than planned time spent in thermal extremes.

It is also vital for the AOCS subsystem to do both sensors-and-attitude-determination closed loop testing and attitude-determination-control-algorithm-feedback-actuator testing

thoroughly, which summarise the core functions of any AOCS system. The testing for both can foreseeably begin in October 2020 on the Engineering Model as by that time the OBCS EM hardware should be ready as well as the procurement of the reaction wheels should be near the end. Some of the testing planned for both of these goals is set out by the Testing Plan presented in Appendix B.

Another important thing to strive for would be the magnetometer calibration and magnetorquer characterisation, for which the author has been setting up a test with Kiwa Inspecta, one of the leading technical control, certification, and testing services provider in Northern Europe. If this fails to take place due to some reason, the AOCS team has the capability to provide preliminary in-house calibration of the magnetometers using the available Helmholtz coils, but this is not as accurate due to a lack of calibrated magnetometers to act as a proven benchmark and much more trust has to be put on the complex accurate theoretical modelling of the magnetic fields inside and around the test setup, which is somewhat outside the aptness of the AOCS team.

The calibration of flight model IMU sensors pre-flight shall encompass the Kiwa Inspecta-aided calibration of the magnetometers and the calibration process of the flight gyroscopes. The measurement and thermal calibration of flight calibration shall take on the same basic form as the process described in Chapter 2, but with a rotation bench equipped with an encoder 40 times more accurate than the one we currently hold. The measurement and thermal calibration of flight accelerometers as well as the thermal calibration of the magnetometers will take on the same exact form as described in this thesis.

3.2.2 Post-launch Flight Model calibration campaign

While it is paramount that the Sun sensors, magnetometers, and gyroscopes reach orbit with calibration parameters as accurate as possible, it is in case of magnetometers almost impossible to account for the magnetic field disturbance caused by the satellite and its various electrical components. Nor is the thermal calibration inside the temperature and climate chamber's iron box as clean as it could be. In any case, the first time the satellite is truly free of any electrical and geological distortions in the magnetic field (which are not part of the final configuration of the satellite) is in orbit. With the planned accuracy of position and orientation determination in orbit, it would be entirely possible to recalibrate the magnetometers in orbit, as described by H.K. Leinweber in his Ph.D. thesis from the Graz University of Technology [29] or numerous

papers published on the topic such as “In-orbit magnetometer bias and scale factor calibration” published in 2016 by C. Hajiyev in the International Journal of Metrology and Quality Engineering [30]. A similar story is with the accelerometer, which can only be calibrated in the presence of 1 g, but nowhere in the smaller part of the scale before reaching orbit. This in-orbit calibration would follow similar guidelines as the one on the ground, with the exception that the satellite body can easily be rotated around almost any axis, with or without constant torqueing. to preserve the rotation axis. The rotation causes a centripetal force on the accelerometer, which can also be theoretically calculated from its position relative to the center of mass and the theoretical acceleration it should feel. The accelerations achieved by this calibration won’t be large but should be more in the ballpark of the accelerations we will witness with the cold gas propulsion thrusts.

Another thing the satellite can self-calibrate for in orbit, or for us to try to analyse on the ground, is to determine the alignment of the coordinate frame of each sensor and actuator with the satellite one. This can be achieved by logging and comparing the outputs of each of the sensors with the expected values and to compare the attitude change with the torques applied to the satellite by each of the actuators.

Conclusions

This thesis set the framework for ESTCube-2 nanosatellite Attitude and Orbit Control Subsystem qualification testing and calibration. One of the outputs of this thesis was the reorganisation of the requirements for the AOCS subsystem to verify AOCS development is in total alignment with mission goals. This was extended upon by the decomposition of said requirements into a more manageable AOCS testing plan, separate for sensors and actuators, which includes the preliminary qualification testing of the sensors and actuators carried out from the beginning of May 2020 and which will last until October of the same year. At that point, ESTCube-2 Flight Model qualification and calibration shall begin.

With Flight Model calibration in mind, this thesis set out to create a template procedure for later IMU sensor calibration, that could be used for every 3-axis MEMS sensor on the Flight Model. This was also achieved by the general sensor model calibration in Chapter 2, which demonstrably refined the sensor results accounting for each orientation and axis using a gain matrix and a bias (or offset) vector; and which was extended to a wider temperature range.

Development of ESTCube-2 is rapidly approaching its final phases before delivery and launch, and the AOCS subsystem shows readiness for conducting a successful and meaningful science experiment.

Acknowledgements

First and foremost I would like to thank my friend and colleague Robert Märk, without whom the testing campaign presented in thesis would have been a more dry and boring version of itself and not nearly as satisfying, and who has been, through the long years, throwing more and more kindling into the fire that drives me to pursue the delicate art of physics.

I would also like to thank my supervisors Dr Riho Vendt and Hendrik Ehrpais for sticking with me and seeing me through even though the World of 2020 decided to go up in flames. I would've been at a complete loss on many occasions if it had not been for Kristo Allaje and the rest of the small team at ESTCube, that came to my aid when in need. My thanks also goes to Ayush Jain, Joel Kuusk and Ilmar Ansko from TO. And lastly, I would like to thank Kirke for putting up with an overworked shadow of a man.

References

[1] M. Swartwout, PhD, CubeSat database. URL:https://sites.google.com/a/slu.edu/swartwout/home/cubesat-database

[2] M. Nowak et al, Short life and abrupt death of PicSat, a small 3U CubeSat dreaming of exoplanet detection. DOI:10.1117/12.2313242

[3] C. C. Venturini, Improving Mission Success of CubeSats, AEROSPACE REPORT NO. TOR-2017-01689.

[4] ECSS, Active Standards. URL:https://ecss.nl/standards/active-standards/

[5] I. Iakubivskyi, P. Janhunen et al, Coulomb drag propulsion experiments of ESTCube-2 and FORESAIL-1, Acta Astronautica (2019), DOI:10.1016/j.actaastro.2019.11.030

[6] IOD/IOV programme for Horizon2020. CORDIS. URL: https://cordis.europa.eu/programme/id/H2020_COMPET-05-2014

[7] ECSS standard for testing. ECSS-E-ST-10-03C. Active, 01 June 2012.

[8] ECSS standard for AOCS. ECSS-E-ST-60-30C. Active, 30 August 2013.

[9] TEB, Tailored ECSS Engineering Standards for In-Orbit Demonstration CubeSat Projects. 24 November 2016. Issue 1 Rev 3. Ref:TEC-SY/128/2013/SPD/RW

[10] Photo Emission Tech Inc. SS150AAA Solar Simulator datasheet. URL: http://www.photoemission.com/techspecs/SS150AAA_Solar_Simulator_Rev._E_Specs.pdf

[11] T. Fiore, ALTA Thermal vacuum system user manual. DOC. No: ALTA/TVS/TN-03, Issue/Ver 1.0, Date:18/07/2013.

[12] Weiss WKL 64/40 datasheet. URL:http://www.omniray.fi/userData/omniray/docs/Weiss-lampo-ja-saa-1.1.pdf

[13] A. Scholz et al. Flight results of the COMPASS-1 picosatellite mission. Acta Astronautica 2010. DOI:10.1016/j.actaastro.2010.06.040

[14] A. Slavinskis, H. Ehrpais et al. Flight Results of ESTCube-1 Attitude Determination System. Journal of Aerospace Engineering, Jan 2016. DOI:10.1061/(ASCE)AS.1943-5525.0000504

[15] Zortrax M200 3D-printed datasheet. URL: https://support.zortrax.com/m-series-specification/

[16] M. K. Nigol. BSc thesis. ESTCube-2 attitude and orbit control system sensor selection and temperature calibration, 2017. URL: http://hdl.handle.net/10062/57437

[17] A. Parelo, BSc thesis. Development of ESTCube-2 side panels, 2018. URL: http://hdl.handle.net/10062/60706

[18] Hamamatsu S9226 CMOS linear image sensor datasheet. URL: https://www.hamamatsu.com/resources/pdf/ssd/s9226_series_kmpd1121e.pdf

[19] LIS3MDL three-axis magnetometer datasheet. URL: https://www.st.com/resource/en/datasheet/lis3mdl.pdf

[20] BMG160 three-axis gyroscopes datasheet. URL: https://www.mouser.com/datasheet/2/783/BST-BMG160-DS000-09-1221199.pdf

[21] FXOS8700CQ three-axis accelerometer datasheet. URL: https://www.nxp.com/docs/en/data-sheet/FXOS8700CQ.pdf

[22] H. Ehrpais, MSc thesis. ESTCube-2 attitude and orbit control system design, 2017. URL: http://hdl.handle.net/10062/56543

[23] A. Slavinskis, H. Ehrpais et al. Flight Results of ESTCube-1 Attitude Determination System. Journal of Aerospace Engineering, Jan 2016. DOI:10.1061/(ASCE)AS.1943-5525.0000504

[24] RW210.15 reaction wheels datasheet: URL:https://hyperiontechnologies.nl/wp-content/uploads/2019/11/HT_RW210.pdf

[25] NanoProp CGP3 datasheet URL: https://gomspace.com/UserFiles/Subsystems/flyer/gomspace_nanoprop_cgp3.pdf

[26] J. Viru, BSc thesis. Design and testing of attitude determination sensors for ESTCube-1, 2013. URL: http://hdl.handle.net/10062/30985

[27] SciPy Differential Evolution library. URL: https://docs.scipy.org/doc/scipy/reference/generated/scipy.optimize.differential_evolution.html

[28] M. Kok et al. Calibration of a magnetometer in combination with inertial sensors. Conference paper, 15th International Conference on Information Fusion, 2012.

[29] H. K. Leinweber, PhD thesis. In-flight Calibration of Space-borne Magnetometers, 2011. URL:https://diglib.tugraz.at/download.php?id=576a7ce7924d5&location=browse

[30] C. Hajiyev. In-orbit magnetometer bias and scale factor calibration, International Journal of Metrology and Quality Engineering, 2016. DOI:10.1051/ijmqe/2016003

Appendices

Appendix A

EC-2 AOCS-specific requirements

EC-2 AOCS REQUIREMENTS

Prepared by: HANS TERAS 	**Date:** AUGUST 16, 2020 **Version:** v1.0

KEY:	
0xx - GENERAL AOCS REQUIREMENTS **1xx - SENSOR REQUIREMENTS** 11x - Magnetometers (MAG) 12x - Gyroscopes (GYR) 13x - Accelerometers (ACC) 14x - Sun Sensor HW (SUN) 15x - Sun Sensor SW (SUN) 16x-19x - General Sensor Requirements **2xx - STAR TRACKER REQUIREMENTS**	**3xx - ACTUATOR REQUIREMENTS** 31x - Reaction Wheels (RW) 32x - Cold Gas Thrusters (CGT) 33x - Magnetorquers (MTQ) **4xx - CONTROL REQUIREMENTS** **5xx - DETERMINATION REQUIREMENTS** **6xx - TESTING EQP. REQUIREMENTS** 63x - Sun sensor testing (SST) 64x - Rotating Bench (RTB)

VERSION	DATE	NAME	CHANGELOG
v1.0	AUG 16 2020	HANS TERAS	First Issue

REQ,	SOURCE	GENERAL / DESCRIPTION
R-AOCS-001	**R-ENV-010**	EC-2 AOCS will operate at temperatures ranging from -20°C to 40°C.
R-AOCS-002	**R-ENV-011**	EC-2 AOCS shall be capable of withstanding temperatures from -30°C to 60°C without any permanent effect.
R-AOCS-003	**R-ENV-020**	EC-2 AOCS shall withstand an ESA Vega-C launch profile - acceleration, environment and vibrations.
R-AOCS-004	**R-CDP-010**	EC-2 AOCS shall be capable of operating at LEO altitudes up to 700 km on a Sun synchronous orbit.
R-AOCS-005	**R-CAM-010**	EC-2 AOCS shall provide attitude stability of 0.125 $\text{deg} \cdot \text{s}^{-1}$.
R-AOCS-006	**N/A**	EC-2 AOCS shall be redundant so failure in any one sensor or actuator shall prevent main objective.
R-AOCS-007	**N/A**	EC-2 AOCS shall have algorithms able to run on STM32F7.
REQ,	**SOURCE**	**SENSORS / DESCRIPTION**
R-AOCS-101	**N/A**	Sensors shall be redundant.
R-AOCS-104	**R-FUN-030**	Sensors shall not exceed 0.5 W peak power usage.
R-AOCS-102	**R-CDP-020** **R-AOCS-011**	Sensor resolution shall be small enough to provide the UKF with data for a cumulative pointing error less than 3°
R-AOCS-103	**R-CDP-060** **R-AOCS-013**	Sensor resolution shall be small enough to make the UKF capable of estimating a change in the magnitude of angular velocity of at least 0.1 $\text{deg} \cdot \text{s}^{-1}$ over two polar passes (or approx, 90 minutes)
R-AOCS-105	**N/A**	All sensors shall use SPI.
R-AOCS-106	**N/A**	All sensors shall use 3.3 V.
R-AOCS-107	**N/A**	All sensors shall have temperature calibration.
R-AOCS-108	**N/A**	All sensors shall have preliminary measurement calibration before launch.
R-AOCS-109	**N/A**	All sensors shall measure faster than 10 Hz.
R-AOCS-161	**N/A**	Sensor data shall be possible to be logged for analysis on the ground.

R-AOCS-161	**N/A**	Sensors shall be housed on OBCS PBC and 6 side panel PCBs.
R-AOCS-141	**N/A**	Sun sensors shall have a field-of-view of at least ±45 deg in two axes.
R-AOCS-142	**N/A**	Sun sensors should have a field-of-view of at least ±55 deg in two axes.
R-AOCS-143	**N/A**	Sun Sensors shall have measurement frequency of 10 Hz or greater.
R-AOCS-143	**R-PHY-020**	Sun sensor height shall be under 4 mm.
R-AOCS-151	**N/A**	Sun sensors should have a Sun vector determination accuracy of less than 0.5 deg.
R-AOCS-151	**N/A**	Sun sensors shall have a dedicated MCU for initial image processing.
REQ.	SOURCE	ACTUATORS / DESCRIPTION
R-AOCS-331	**R-FUN-030**	Magnetorquers shall not exceed 4 W peak power usage per coil.
R-AOCS-332	**R-PHY-020**	Magnetorquer size shall be under 250 x 67 mm on long sides and 83 x 80 mm on the short.
R-AOCS-311	**R-PHY-020**	Reaction wheels shall not exceed 25 x 25 x 15 mm in size.
R-AOCS-333	**N/A**	Magnetorquers shall use 10 V from the regulator.
R-AOCS-334	**N/A**	Magnetorquers shall provide at least 0.5 Am^2 of magnetic moment.
R-AOCS-301	**R-CDP-020**	Actuators shall provide enough angular momentum for the CDP experiment to deploy the first 11 meters of tether.
R-AOCS-302	**R-CDP-120**	Actuators shall be able to compensate for the residual magnetic torque caused by the micro-tether unwinding motor.
R-AOCS-321	**R-PHY-020**	Cold Gas Propulsion module shall be under 0.3 U.
REQ.	SOURCE	CONTROL / DESCRIPTION
R-AOCS-401	**R-CDP-050**	EC-2 AOCS shall keep the tether tension between 3 and 30 mN while CDP experiment is ongoing.
R-AOCS-402	**R-CDP-021**	EC-2 AOCS shall provide spin axis alignment with the Earth's polar axis with a pointing error less than 3° for the CDP experiment.

R-AOCS-403	**N/A**	AOCS shall be able to perform in 5 different configurations: 1) MTQ, 2) RW, 3) MTQ+RW, 4) MTW+RW+CGP, 5) RW+CGP
REQ.	SOURCE	DETERMINATION / DESCRIPTION
R-AOCS-501	**R-CDP-060**	EC-2 AOCS shall be capable of determining a change in the magnitude of angular velocity of at least 0.1 deg $\cdot s^{-1}$ over two polar passes (or approx, 90 minutes)
R-AOCS-502	**R-CDP-070**	EC-2 AOCS shall be capable of estimating a change in the orbital altitude of at least 10 km over six months from the start of the Coulomb drax experiment.
R-AOCS-503	**N/A**	UKF shall run faster than 4 Hz.
REQ.	SOURCE	DESCRIPTION
R-AOCS-631	**N/A**	Sun Sensor test bench shall be adjustable in two axes.
R-AOCS-641	**N/A**	Rotating bench shall have an encoder.
R-AOCS-642	**N/A**	Rotating bench shall have capability to be spun up to 360 deg/s.

Appendix B

EC-2 AOCS Testing Plan

EC-2 AOCS TESTING PLAN

Prepared by: HANS TERAS 	**Date:** AUGUST 15, 2020 **Version:** v1.2

KEY	CATEGORIZATION
1 - SENSORS 1.1.xyz - Magnetometers (MAG) 1.2.xyz - Gyroscopes (GYR) 1.3.xyz - Accelerometers (ACC) 1.4.xyz - Sun Sensor HW (SUN) 1.5.xyz - Sun Sensor SW (SUN) **2 - STAR TRACKER** **3 - ACTUATORS** 3.1.xyz - Reaction Wheels (RW) 3.2.xyz - Cold Gas Thrusters (CGT) 3.3.xyz - Magnetorquers (MTQ) **4 - CONTROL SW** **5 - DETERMINATION SW** **6 - TESTING EQ** 6.3.xyz - Sun Sensor Test bench (SST) 6.4.xyz - Rotating Bench (RTB)	**x - TESTED MODEL** 1 - Prototype 2 - Engineering Model / FlatSat 3 - Flight Model **y - TEST TYPE** 1 - Functionality 2 - Thermal 3 - Vacuum 4 - Thermal Vacuum 5 - Vibration 6 - Shock 7 - Software **z - TEST NUMBER**
IMU - 1.0.xyz, **Inertial Measurement Unit** (inc. MAG, GYR, ACC)	**Roman numeral** - Repeated test

VERSION	DATE	NAME	CHANGELOG
1.0	JUN 03, 2020	HANS TERAS	First Issue
1.1	AUG 06, 2020	HANS TERAS	1) Categorized and updated sensor tests 2) Added some Flight model sensor tests 3) Added actuator and misc tests
1.2	AUG 15, 2020	HANS TERAS	1) Updated done sensor tests 2) Added sensor testing campaign for autumn 2) Added actuator testing campaign for autumn 3) Added Flight Model qualification tests for sensors and actuators

REQUIREMENTS AND DESCRIPTIONS LISTED IN appendix A: "EC-2 AOCS REQUIREMENTS".

SENSORS					
Dsgnt.	Test no.	Req. no.	Description	Date	Status/Result
IMU	1.0.111	N/A	General Functionality Tests	May, 2017	Done. Performed by Madis Kaspar Nigol as part of sensor selection BSc thesis.
IMU	1.0.221	R-ENV-010	Thermal Working Range Functionality Test	Aug 05, 2020	Done. Passed.
IMU	1.0.222	R-ENV-011	Thermal Max Range Withstand Test	Aug 06, 2020	Done. Passed.
IMU	1.0.231	R-CDP-010	Low Vacuum Effects Calibration	Aug 06, 2020	Done. Due to mechanical noise, needs to be retested in high vac with the satellite.
IMU	1.0.232	R-CDP-010	High Vacuum Withstand Test	Aug 04, 2020	Done. Passed.

IMU	1.0.251	N/A	RW operation vibration noise test.	Aug 11, 2020	Done. Data to be analysed.
IMU	1.0.211	R-CDP-021	Zero-G Stratospheric Drop Test	SEPT, 2020 ?	Planned with TalTech Robotics Club.
IMU	1.0.341	R-ENV-010 R-ENV-011 R-CDP-010	IMU Thermal Vacuum Capability Test	DEC, 2020	FLIGHT MODEL CAMP.
IMU	1.0.351	R-ENV-020	IMU Vega Flight Profile Vibration Test	OCT, 2020	FLIGHT MODEL CAMP.
IMU	1.0.361	R-ENV-020	IMU Shock Withstand Test	OCT, 2020	FLIGHT MODEL CAMP.
MAG	1.1.211	R-CDP-021	Stationary Earth Magnetic Field Strength Calibration	July 18, .2020	Done. Gives a rough estimate of sensor hard and soft iron biases.
MAG	1.1.212	R-CDP-021	Industrial Helmholtz Magnetometer Calibration	AUG, 2020	Skipped for 1.1.311
MAG	1.1.311	R-CDP-021	Flight Model Magnetometer Calibration in Kiwa	NOV, 2020	FLIGHT MODEL CAMP. Planned with Kiwa/Inspecta
GYR	1.2.221	R-CAM-010 R-CDP-060	Gyroscope Slow Rotating Bench Thermal Calibration	July 28, 2020	Done. Calibration functions in thermal working range (from -20℃ to 40℃) at 20℃ intervals for angular velocities 0 to 20 deg/s .
GYR	1.2.222	R-CAM-010 R-CDP-020 R-CDP-060	Gyroscope Fast Rotating Bench Thermal Calibration	AUG, 2020	Calibration functions in thermal working range (from -20℃ to 40℃) at 20℃ intervals for angular velocities 30 to 360 deg/s .

GYR	1.2.311	R-CAM-010 R-CDP-060	Flight Model Gyro Calibration	NOV, 2020	FLIGHT MODEL CAMP.
ACC	1.3.211	N/A	Gravitational Acceleration Thermal Calibration	Aug 11, 2020	Done. Data analysed. Generic calibration for preliminary flight operations. Refined calibration in orbit.
SUN	1.4.111	R-DES-020 R-CDP-010	Sensor Reflective Film Prototyping	JUNE, 2019 - JUNE, 2020	Done, sufficient Ti layer found, needs verification in production consistencies.
SUN	1.4.112	R-SS-010	Sensor Field of View Mask Slit Width Test	July 24, 2019	Done. 100 um slit selected for FoV capabilities.
SUN	1.4.113-I	R-CDP-010	Film Thickness Consistency Solar Sim. Test 1	June 12, .2020	Done, inconsistencies in production and/or transport. Needs re-testing.
SUN	1.4.113-II	R-CDP-010	Film Thickness Consistency Solar Sim. Test 2	July 1, 2020	Done. Consistent results. Ordered the rest.
SUN	1.4.211	R-CDP-021	Sensor Functionality Demonstration in Atmosphere	June 17, .2020	Test passed.
SUN	1.4.212	R-CDP-021	Solar Sim. Field of View Test	July 1, 2020	Test done. Sufficient FoV range detected.
SUN	1.4.213	R-CDP-021	Solar Sim. Rotating Table Field of View Test	JUL,2020	Test skipped for 1.4.214
SUN	1.4.214	R-CDP-021	Two-Axis Intensity Calibration	Aug 7-8, .2020	Test done. Error data and accuracy to be analysed. FoV measured for 1.4.214.
SUN	1.4.221	R-ENV-010	Thermal Working Range Functionality Test	05.08.2020	Test done. No defects encountered after running

					60 minutes in working range extremes with intermittent data collection.
SUN	1.4.222	R-ENV-011	Thermal Max Range Withstand Test	06.08.2020	Test done. No defects encountered after 60 minutes in thermal withstand extremes while shut down.
SUN	1.4.223	R-ENV-011	Thermal Influence Calibration	AUG, 2020	Figure out a light source. 3 small diodes, uncoated sensor.
SUN	1.4.231	R-CDP-010	Low Vacuum Influence Calibration	AUG, 2020	Skipped for 1.4.232
SUN	1.4.232	R-CDP-010	High Vacuum Withstand Test	SEPT 2020	
SUN	1.4.311	R-CDP-021	Flight Model Sensors Alignment	DEC, 2020	FLIGHT MODEL CAMP.
SUN	1.4.341	R-ENV-010 R-ENV-011 R-CDP-010	Thermal Vacuum Testing	DEC, 2020	FLIGHT MODEL CAMPAIGN
SUN	1.4.351	R-ENV-020	Sun Sensor Vega Flight Profile Vibration Test	NOV, 2020	FLIGHT MODEL CAMP.
SUN	1.4.361	R-ENV-020	Sun Sensor Shock Test	NOV, 2020	FLIGHT MODEL CAMP:
SUN	1.5.271	N/A	Side Panel Data Flow Test	SEPT, 2020	Waiting for SP ENG HW.
SUN	1.5.371	N/A	Side Panel Closed Loop Data Flow	OCT, 2020	FLIGHT MODEL CAMP.

ACTUATORS					
Dsgnt.	Test no.	Req. no.	Description	Date	Status/Result
RW	3.1.111	N/A	General Functionality Test on Arduino/EGSE	Jul. 20, 2019	OK. Some connector wires loosened. Returned to the manufacturer. Connectors redone. OK
RW	3.1.211	N/A	RW Operations Sensor Disturbance Test	Aug 11, 2020	Done. Data to be analysed.
RW	3.1.271	R-AOCS-007	RW Control Using OBCS	AUG, 2020	Driver development started.
RW	3.1.212	R-CDP-020	Torque-testing RW with control algorithms using Arduino.	SEPT, 2020	Figure out 3D frame for mounting, frame fixture and balancing.
RW	3.1.272	R-CAM-010	Simple closed-loop RW test with Arduino and sensor-board	SEPT, 2020	Software to be written.
RW	3.1.213	R-CDP-021	Closed-loop testing of RW with OBCS and sensors.	OCT, 2020	Waiting for OBCS ENG HW.
RW	3.1.311	N/A	Functionality testing Flight Model RWs	NOV, 2020	FLIGHT MODEL CAMP.
RW	3.1.371	R-CAM-010	Closed-loop testing RWs in AOCS algos	DEC, 2020	FLIGHT MODEL CAMP.
RW	3.1.312	N/A	Desaturating tests with MTQ	NOV, 2020	FLIGHT MODEL CAMP.
MTQ	3.3.211	R-AOCS-334	General Functionality Test for Coil Driver	SEPT, 2020	Waiting for SP ENG HW.
MTQ	3.3.221	R-AOCS-333	Thermal calibration of Coil Driver and Coil	OCT, 2020	Waiting for SP ENG HW.
MTQ	3.3.271	N/A	Magnetorquer Control Using OBCS	SEPT, 2020	Waiting for SP ENG HW.

MTQ	3.3.212	R-CDP-021	Closed-loop testing of MTQ with OBCS and sensors.	OCT, 2020	Waiting for FlatSat
MTQ	3.3.311	N/A	Functionality testing Flight Model MTQs	NOV, 2020	FLIGHT MODEL CAMP.
MTQ	3.3.371	R-CAM-010	Closed-loop testing MTQs in AOCS algos	DEC, 2020	FLIGHT MODEL CAMP.
CGT	3.2.311	N/A	General functionality test.	OCT, 2020	Needs OBCS ENG HW, SW and fuel.
CGT	3.2.312	R-CDP-020	Closed-loop testing CGP in AOCS algos	DEC, 2020	FLIGHT MODEL CAMP.

MISCELLANEOUS

Dsgnt.	Test no.	Req. no.	Description	Date	Status/Result
SSTB	6.3.211	R-AOCS-631	Sun sensor test bench operational in 2-ax.	Aug 7, 2020	Done.
RTB	6.4.111	N/A	General Functionality Test	25.08.2019	Done. HW and SW work.
RTB	6.4.211	R-CAM-010 R-CDP-060	Rotating Bench Noise and Uncertainty Test, 90 cogs.	11.07.2020	Done.Used 90 cog wheel.

Appendix C

Test protocols

C.1 - 6.4.221 - Rotating Bench Noise and Uncertainty Analysis

C.2 - 1.0.221 / 1.4.221 - Sensor Thermal Working Range Functionality Test

C.3 - 1.0.222 / 1.4.222 – Sensor Thermal Max Range Withstand Test

TESTING PROTOCOL

DATE	July 11, 2020	ESTCUBE-2	PROJECT
LOCATION	TARTU OBSERVATORY	AOCS	SUBSYSTEM
ENGINEER	HANS TERAS	RTB	DESIGNATION
TEST NO.	6.4.221	R-CAM-010 R-CDP-060	REQ NO.
TEST DESCRIPTION	Rotating Bench Noise and Uncertainty Analysis	Rotating Bench w/ Arduino Nano and optical switch Power Supply	EQUIPMENT

1 TEST GOAL

Goal is to measure the noise of the readings caused by the stepper motor and optical switch setup. This allows us to calculate the type A and type B uncertainties for the estimation of the angular velocity of the sensor board on top of the rotating bench.

2 TEST DESCRIPTION

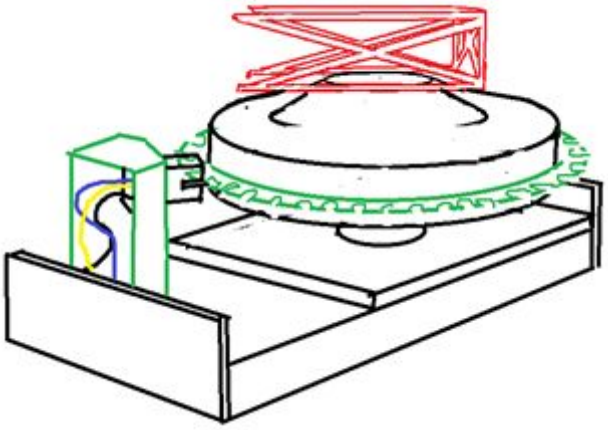

Rotating bench setup with the driving motor and transmission missing.

Mount the sensor testing frame onto the rotating bench to simulate future loads. Hook up the rotating bench to the power supply set to 0 V. Start graphing the instantaneous and noisy values of angular velocity read/calculated by the Arduino. Increase and tune the voltage output of the power supply until the noise seems to be centered around a certain value under consideration. Mark down the respective voltage for future reference.

The values under consideration are 30 deg/s, 60 deg/s, 90 deg/s, 120 deg/s, 180 deg/s, 360 deg/s and 720 deg/s. Log a set amount of readings on each different velocity (around 1000).

Graph the following datasets shifted to their mean. Calculate the standard deviations and respective margins of error. Measure and calculate 3D gear dimensions and calculate type B uncertainty. Calculate rotating bench combined uncertainty.

3 TEST OUTCOME + DATA

Sample dataset at 30 deg/s. Graph y-axis shows the deviation from mean at ~30 deg/s.

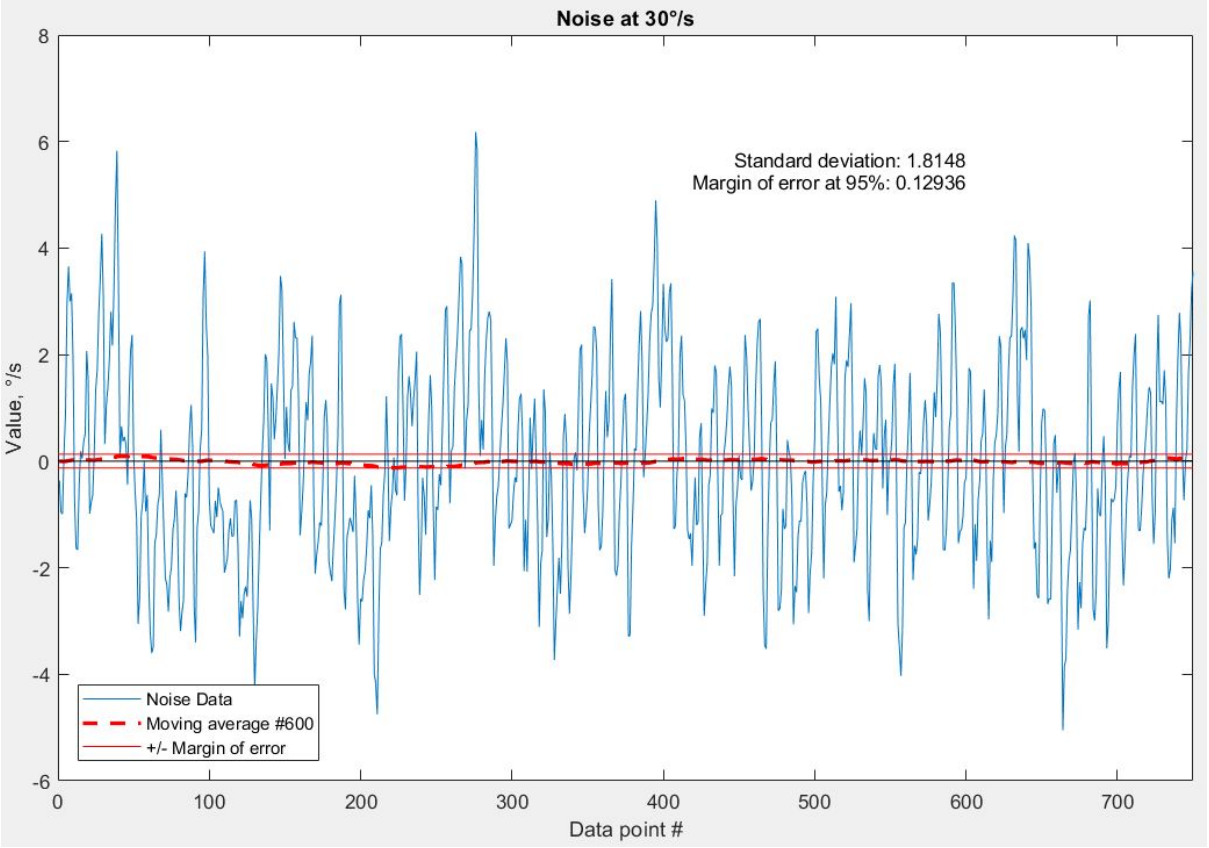

Every dataset was truncated to **N** = 750 data points. The mean (**μ**) of the dataset was calculated and subtracted from the dataset to plot the noise around mean. Next, the margin of error or **Type A uncertainty** ($\mathbf{u^A}$) was calculated from the standard deviation ($\boldsymbol{\sigma}$) and the square root of the size of the dataset.

$$u^A = \frac{\sigma}{\sqrt{N}} = \frac{1.8148}{\sqrt{750}} = 6.6399 \cdot 10^{-2}\ deg{\cdot}s^{-1}$$

Then the margin of error was estimated at the 95% confidence level to be $\boldsymbol{U^A = 1.96 \cdot u^A = \pm 0.13°/s}$. A moving average buffer size of 600 was used on the data to make it easier to manage the future testing and to confine the values of the rotating bench within or near the margin of error.

We can also analyse the 3D printed gear dimensional accuracy from the datasheet[1] provided by the 3D printer manufacturer. The datasheet specifies the dimensional accuracy as **±0.2%**. This lets us estimate the uncertainty in cog width and thus in the estimated angle moved and angular velocities.

The measured width of single cog is **2.74 mm**. The gaps between the cogs are **2.44 mm**. The optical switch measures the elapsed time from the the leading edge of one cog until the leading edge of the next one. This gives us a rough distance of **5.18 mm**, which is thus subject to the **0.2%** dimensional

[1] https://support.zortrax.com/m-series-specification/

accuracy of the 3D printer. The real distance is then **5.18 ± 5.18 · 0.002 mm = 5.18 ± 0.01 mm**. To calculate the corresponding angle we use the number of cogs on the gear (**90**), meaning each perfect cog-gap pair would make up an angle of **4°**. Considering that **5.18 mm** corresponds to a perfect angle of **4°** a distance of **5.18 ± 0.01 mm** would correspond to an uncertainty of **4 ± 0.008°** in the angle.

From this we can estimate **Type B uncertainty** ($\mathbf{u^B}$) to be:

$$u^B = \frac{0.008}{\sqrt{3}} = 0.005°$$

and an expanded uncertainty at 95% confidence level to be:

$$U^B = 1.96 \cdot 0.005° = 0.01°$$

This value might seem over 10 times lower than Type A uncertainty, but it's effects come strongly into play with higher angular velocities. For example at 30°/s, U^B is around 7.5 $s^{-1} \cdot 0.01°$ = 0.075°/s but at 360°/s, U^B would grow to approximately 90 $s^{-1} \cdot 0.01°$ = 0.9°/s, which is almost 10 times the size of Type A uncertainty at that velocity: 0.16°/s.

Respective dataset:

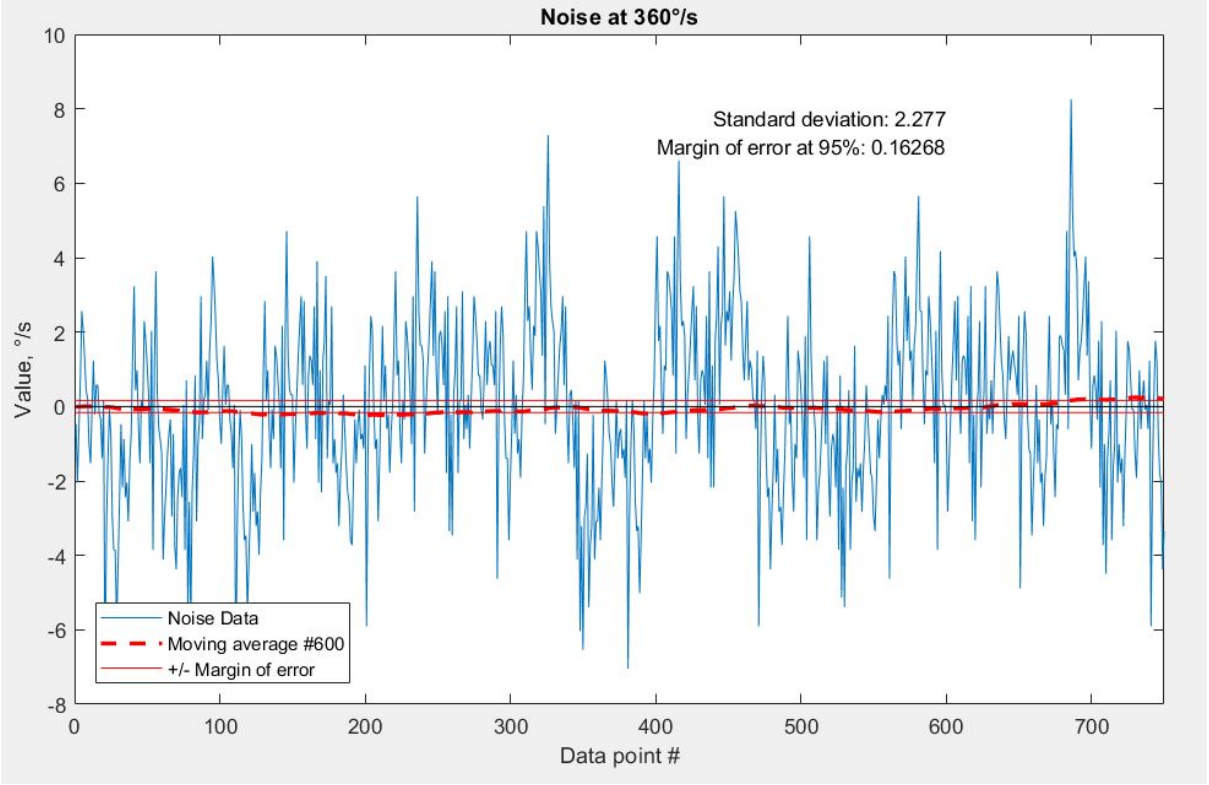

With the gathered data and uncertainty calculations we can fill the following table:

Angular Velocity	Voltage	Expanded Type A uncertainty	Expanded Type B uncertainty	Combined expanded uncertainty
30 deg/s	1.86 V	±0.129 deg/s	±0.075 deg/s	±0.149 deg/s
60 deg/s	2.55 V	±0.127 deg/s	±0.15 deg/s	±0.197 deg/s
90 deg/s	3.26 V	±0.110 deg/s	±0.225 deg/s	±0.25 deg/s
120 deg/s	3.98 V	±0.110 deg/s	±0.3 deg/s	±0.32 deg/s
180 deg/s	5.51 V	±0.118 deg/s	±0.45 deg/s	±0.465 deg/s
270 deg/s	7.79 V	±0.133 deg/s	±0.675 deg/s	±0.688 deg/s
360 deg/s	10.05 V	±0.162 deg/s	±0.9 deg/s	±0.914 deg/s
720 deg/s	19.14 V	±0.272 deg/s	±1.8 deg/s	±1.82 deg/s

Where we have used the following formula to estimate Combined uncertainty:

$$U^C = \sqrt{(U^A)^2 + (U^B)^2}$$

The data clearly follows a linear trend, dominated by linear Type B uncertainty on higher angular velocities and by Type A stepper motor noise and jerking on the lower angular velocities. A function for the latter remains unspecified at the moment as the electric motor lacks torque on low voltages to overcome the static friction of the rotating bench.

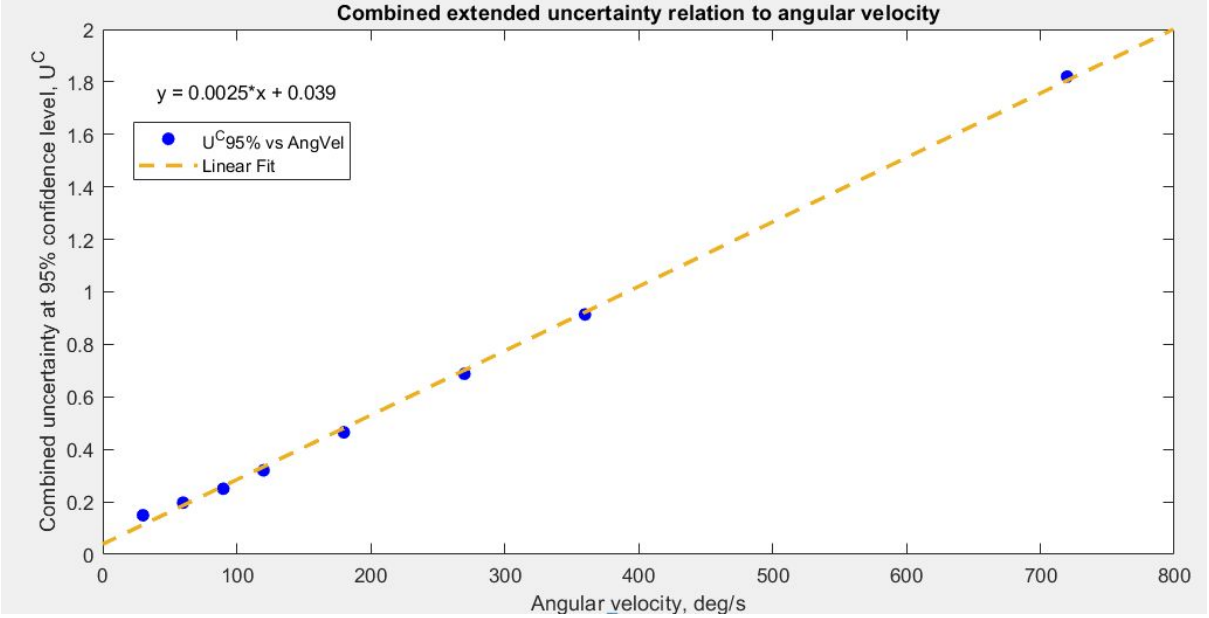

TESTING PROTOCOL

DATE	August 4, 2020	ESTCUBE-2	PROJECT
LOCATION	TARTU OBSERVATORY	AOCS	SUBSYSTEM
ENGINEER	HANS TERAS	IMU / SS	DESIGNATION
TEST NO.	1.0.221 / 1.4.221	R-ENV-010	REQ NO.
TEST DESCRIPTION	Thermal Working Range Functionality Test	Temp. and climate chamber. Rotating bench. AOCS sensor board and 3D printed frame. Sun sensor prototype board.	EQUIPMENT

1 TEST GOAL

This test shall verify that the IMU sensors and Sun sensors encounter no detectable problems or errors during a long duration stress test in the required working temperature range of -20°C to 40°C.

2 TEST DESCRIPTION

The chamber is prepared with the rotating bench inside it. The rotating bench is levelled and connected to the power grid.

A short (1 min) data collection run is performed with the sensors in ambient temperature. This will be the benchmark against which the working range raw data can be compared to. Any larger deviations from this baseline will need to be investigated until a cause for the deviation is pinpointed.

The data collection will be performed in a single off-axis attitude, to get a sensible reading for all sensor axes. The data collection will be 60 minutes in duration, as the time to complete one orbit around the Earth at a Sun-synchronous 500 km LEO is about 90 minutes, meaning that the time spent in eclipse (behind Earth) might vary from 0 to about 30 minutes, depending on the launch profile. The 60-minute stress test amply covers the max envisioned time spent in eclipse and is around the amount of time we configure our satellite to spend in direct sunlight.

The temperature chamber is then heated up to 40°C and the data logging session is performed as temperature stabilises at 40±1°C. The data is logged in four 15-minute intervals as the chamber is opened every 15 minutes for around 10 seconds to

verify a good signal response from the Sun sensor, by bringing a light source over it.

The chamber is then cooled back down to ambient and another short (1 min) control run is performed to make note of any deviations in the data that may or may not have appeared. The temperature chamber is cooled down to -20±1°C and the other data collection run is performed. The chamber is reheated to ambient and a final control run is done to ensure if any deviations in the sensors may be permanent or not.

3 TEST OUTCOME

No problems were spotted during any of the thermal test data collection runs and the test is considered passed. The sensors have no problems working in temperatures ranging from -20 ℃ ±1 ℃. to +40 ℃ ±1 ℃.

4 FURTHER WORK

TESTING PROTOCOL

DATE	July 30, 2020	ESTCUBE-2	PROJECT
LOCATION	TARTU OBSERVATORY	AOCS	SUBSYSTEM
ENGINEER	HANS TERAS	IMU / SS	DESIGNATION
TEST NO.	1.0.222 / 1.4.222	R-ENV-011	REQ NO.
TEST DESCRIPTION	Thermal Max Range Withstand Test	Temp. and climate chamber. Rotating bench. AOCS sensor board and 3D printed frame. Sun sensor prototype board.	EQUIPMENT

1 TEST GOAL

The goal of this test is to ensure that the satellite has the thermal capabilities to withstand the temperature extremes that a spacecraft can experience on a Sun-synchronous LEO orbit and that it's AOCS sensors, both IMUs and Sun sensors, meet those requirements in addition to meeting them on the datasheet.

2 TEST DESCRIPTION

The withstand test will be 60 minutes in duration, as the time to complete one orbit around the Earth at a Sun-synchronous 500 km LEO is about 90 minutes, meaning that the time spent in eclipse (behind Earth) might vary from 0 to about 30 minutes, depending on the launch profile. The 60-minute thermal test amply covers the max envisioned time spent in eclipse and is around the amount of time we configure our satellite to spend in direct sunlight.

The Weiss WKL 64/40 temperature test chamber is heated up to 60 ℃ ±1℃.
Before putting the Sun sensor board and the AOCS sensor board into the temperature chamber, a short verification run is done to ensure normal working modes are active for both sensors and no problems are present.

The sensors are then left inside the chamber for 60+ minutes in stand-by mode, without logging data. After an hour, the sensors are taken out and left to cool to room temperature. Another verification run is done to check if the high thermal extreme caused any issues. If issues are found, the test is stopped and fault is debugged.

If no issues are found, the thermal chamber is cooled down to -40 ℃ ±1℃. and the 60 minute test is repeated with no data logging and the sensors on stand-by.
A final verification run is done at the end to discover any issues.

3 TEST OUTCOME

No problems were encountered, this test is considered passed.

4 FURTHER WORK

N/A

Lihtlitsents lõputöö reprodutseerimiseks ja üldsusele kättesaadavaks tegemiseks

Mina, Hans Teras (12.05.1994),

1. annan Tartu Ülikoolile tasuta loa (lihtlitsentsi) minu loodud teose

“ESTCube-2 asendi määramise ja kontrolli alamsüsteemi sensorite ja täiturite kalibratsioon ja hindamine”

mille juhendajad on Riho Vendt ja Hendrik Ehrpais,

reprodutseerimiseks eesmärgiga seda säilitada, sealhulgas lisada digitaalarhiivi DSpace kuni autoriõiguse kehtivuse lõppemiseni.

2. Annan Tartu Ülikoolile loa teha punktis 1 nimetatud teos üldsusele kättesaadavaks Tartu Ülikooli veebikeskkonna, sealhulgas digitaalarhiivi DSpace kaudu Creative Commonsi litsentsiga CC BY NC ND 3.0, mis lubab autorile viidates teost reprodutseerida, levitada ja üldsusele suunata ning keelab luua tuletatud teost ja kasutada teost ärieesmärgil, kuni autoriõiguse kehtivuse lõppemiseni.

3. Olen teadlik, et punktides 1 ja 2 nimetatud õigused jäävad alles ka autorile.

4. Kinnitan, et lihtlitsentsi andmisega ei riku ma teiste isikute intellektuaalomandi ega isikuandmete kaitse õigusaktidest tulenevaid õigusi.

HANS TERAS

Tartu, 17.08.2020